International Journal of Multiphase Flow 151 (2022) 104043

Contents lists available at ScienceDirect

International Journal of Multiphase Flow

journal homepage: www.elsevier.com/locate/ijmulflow

Atomization and droplet dynamics of a gas-liquid two-phase jet under different mass loading ratios

Hao Wu [a], Fujun Zhang [a], Zhenyu Zhang [a,*], Lin Hou [b]

[a] School of Mechanical Engineering, Beijing Institute of Technology, Beijing 100081, China
[b] State Key Laboratory of High Temperature Gas Dynamics, Institute of Mechanics, Chinese Academy of Sciences, Beijing 100190, China

ARTICLE INFO

Keywords:
Gas-liquid two-phase jet
Mass loading ratio
Stokes number
Breakup
Collision

ABSTRACT

Atomization and droplet dynamics of a gas-liquid two-phase jet were investigated experimentally, with the particular interest in the influence of mass loading ratio (the ratio of droplet mass flow rate to the carrier-phase mass flow rate, ranging from 0.60 to 3.23) on the jet atomization. Droplet size and velocity at selected positions were obtained by employing Phase Doppler Particle Analyzer (PDPA), combined with backlit illumination for spray visualization. Droplet transport characteristics are substantially influenced by the mass load ratio. Characterization of the local gas flow velocity by using droplets smaller than 5 μm reveals a highly turbulent jet with Reynolds number exceeding 5×10^4, implying the possibility of droplet turbulent breakup. Critical equilibrium location x_{crit} between droplet breakup and coalescence is close to the nozzle exit and a positive correlation is found between mass loading ratio and x_{crit}. Exaltation of mass loading ratio increases the droplet size and decreases the velocity. Quantification of droplet collision outcome indicates a relatively high probability of coalescence, which explicates the downstream increasing of measured droplet Sauter mean diameter along the centerline of far-field jet.

1. Introduction

Atomization of liquid jet is a classical concept in the domain of fluid mechanics with a wide range of engineering applications (Lefebvre and McDonell, 2017). Spray formation is a common phenomenon in a variety of scientific and engineering applications. In general, atomization process in the spatial domain is perceived into two regimes, namely, the primary atomization regime in the near field and the secondary atomization regime in the far field (Lin and Reitz, 1998; Rajamanickam and Basu, 2016). Classical studies reported primary atomization as an instability driven phenomenon (Gorokhovski and Herrmann, 2008). For instance, the Rayleigh–Taylor (RT) instabilities that arise when there is unfavorable density stratification and Kelvin–Helmholtz (KH) instabilities that occur due to differences in velocities across the liquid-gas interface (Beale and Reitz, 1999; Kourmatzis and Masri, 2014; Reitz and Liu, 1993; Vadivukkarasan and Panchagnula, 2016; Varga et al., 2003). Secondary atomization, on the other hand, is described as the process of further formation of much smaller droplets from filaments, larger blobs, and droplets generated by primary atomization (Guildenbecher et al., 2009).

Depending on the type of fluid involved, atomization can be generally divided into single-fluid type and twin-fluid type (Saha et al., 2012; Wu et al., 2021a). Atomization of a single-fluid is accomplished by discharging a high-pressure fluid via a plain orifice (Wang and Fang, 2015; Wang et al., 2019). Therefore, single-fluid atomization is strongly reliant on the pressure difference between the fluid inside the nozzle and the surrounding ambience, which necessitates the establishment of suitably high fluid pressure and a guaranteed flow rate (Sharma and Fang, 2015). By contrast, the twin-fluid atomization substantially enhances atomization quality via forced aerodynamic instability by using gas streams or jets under quite low pressure (Wu et al., 2020b; Zaremba et al., 2017). Previous investigations indicate twin-fluid atomization is based on the high shear stresses that develop at the liquid-gas interface (Bayvel, 1993). Consequently, two-phase jets inherently involve a large range of physical scales since one generally identifies different regimes according to the topology and the geometry of the interfaces separating two fluids (Drui et al., 2019). Owing to the presence of additional gas, the twin-fluid atomization and resultant spray essentially point to a relatively complex multi-phase flow issue involving stochastic nature of carrier-phase turbulence and polydispersity of dispersed-phase

* Corresponding author.
E-mail address: zhenyu.zhang@bit.edu.cn (Z. Zhang).

https://doi.org/10.1016/j.ijmultiphaseflow.2022.104043
Received 20 July 2021; Received in revised form 18 December 2021; Accepted 3 March 2022
Available online 7 March 2022

distribution (Balachandar and Eaton, 2009). In spite of the experimental discoveries (Urbán et al., 2017; Wu et al., 2021a; Zaremba et al., 2017) and theoretical advances (Jiang et al., 2010; Lasheras et al., 1998; Reitz and Liu, 1993; Varga et al., 2003) made in the past decades, our understanding of the fundamental processes of twin-fluid atomization is far from being complete.

In light of the location where the contact between the gas and liquid phases occurs, the atomization of two-phase jets can be further categorized into internal-mixing and external-mixing types (Lefebvre and McDonell, 2017; Wu et al., 2021a). The external-mixing types, such as air-blast atomizers, are more frequent in coaxial jets and have a wide range of applications in gas turbine and propellant systems (Kourmatzis and Masri, 2014). Internal-mixing twin-fluid atomization, on the other hand, is more commonly used in industrial spray applications as well as piston internal combustion engines. When it comes to internal-mixing twin-fluid sprays, effervescent atomization must be mentioned, which has been well summarized by Sovani et al. (2001). The gas phase is bubbled into the bulk liquid through numerous aerators to establish a bubbly two-phase mixture upstream therefore jet atomization is promoted by bubbly explosion (Jedelsky and Jicha, 2013). As the two-phase mixture passes through the exit orifice, gas bubbles expand rapidly and shatter the liquid into smaller fractions (Zaremba et al., 2017). Effervescent atomization is characterized mostly by its insensitivity to fluid rheological properties and low gas consumption. However, when the gas phase concentration is relatively high, the two-phase flow progressively evolves into another form, namely, a droplet-laden jet (a.k.a., liquid-laden jet) (Ferrand et al., 2003; Lau and Nathan, 2014), which is of interest in the present study.

Droplet-laden jet, typically consisting of liquid droplet suspended in a carrier phase (normally air) flow, is an important category for gas-liquid two-phase jets because it is widely associated with many applications, e.g., aerosol transport and spray combustion (Lau and Nathan, 2014; Mashayek and Pandya, 2003). The carrier phase flow may be in a laminar or turbulent regime. Admittedly, the turbulent regime makes the problem even more complicated since it involves the complex droplet-flow interactions that strongly influence the fuel droplet distributions hence flame instability (Ferrand et al., 2003; Jebakumar and Abraham, 2016). Despite significant attempts to comprehend these issues, the droplet-laden jets continue to provide a challenge to engineers and physicists in developing the analytical description.

In combustion systems, accurate statistical description of spray droplet behavior contributes to an in-depth understanding of droplet phase transitions, rates of evaporation, mixing with oxidizing gas and combustion (Williams, 2018). To describe the droplets in the spray for mathematical convenience, a statistical description function is usually given by $f(r,x,v,t)drdxdv$, which represents the average droplet number at time t over droplet radius range $[r,r+dr]$, intervals of Euclidean space $[x,x+dx]$ and droplet velocity range $[v,v+dv]$. Noted that dx and dv are abbreviations for the three-dimensional elements of physical space and velocity space, respectively. Based on this function, a spray transport equation describing the evolution of $f(r,x,v,t)$ may be derived by using reasoning analogous to those employed in the gas kinetic theories (Lasheras et al., 1998).

$$\frac{\partial f}{\partial t} = -\frac{\partial}{\partial r}(Rf) - \nabla_x\cdot(vf) - \nabla_v\cdot(\boldsymbol{F}f) + Q_b^{'} + \Gamma_c^{'} \tag{1}$$

where $\boldsymbol{F} = d\boldsymbol{v}/dt$ represents the force per unit mass acting on a liquid droplet, $R = dr/dt$ is the changing rate of the droplet size r at (r,x,v,t), and the subscripts on the gradient operators distinguish derivatives to spatial and velocity coordinates. $Q_b^{'}$ is the time rate of increase of f due to droplet breakup and $\Gamma_c^{'}$ represents the changing rate of f caused by droplet collision. However, it is quite difficult to collect information about each droplet within a spray to obtain a distribution function. Consequently, an effective solution is to construct a reasonable distribution function by sampling enough droplets with experimental methods. As a result, the spray/droplet behavior and associated characteristics may be analyzed by further statistical calculations (Feng et al., 2019).

Numerous studies (Lasheras and Hopfinger, 2000; Lasheras et al., 1998; Varga et al., 2003; Wu et al., 2021a) demonstrate that both droplet breakup and collision exist in the two-phase jet. Therefore, a considerable number of studies (Jiang et al., 1992; Qian and Law, 1997; Tang et al., 2012; Zhang et al., 2016; Zhang and Zhang, 2017) have been carried out on the droplet dynamics and collision-coalescence mechanism, emphasizing the fundamental physics of binary droplet collision and its influences on spray flow in practical applications (Saha et al., 2012; Sommerfeld and Pasternak, 2019; Wu et al., 2020b). Contrary to atomization that promotes droplet size reduction, droplet collision is more likely to cause droplet coalescence, which in turn increases droplet size.

Earlier studies on droplet collision study were primarily concerned with the collision between water droplets and the examination of their terminal velocities (Brazier-Smith et al., 1972; Orme, 1997). These studies proposed the collision regime map in the parameter space of impact parameter B and collision Weber number We_c to describe the transition boundary of coalescence and separation for equal-sized water droplet collision. The collision regime monogram was further expanded under the experimental results of hydrocarbon droplets (Qian and Law, 1997) for both equal and unequal sizes (Tang et al., 2012). For hydrocarbon droplets, five distinguishable regimes of collision outcomes, namely, soft coalescence (I), bouncing (II), hard coalescence (III) and coalescence followed by separations (IV and V) are usually observed. Although droplet collision dynamic has been extensively recognized in a

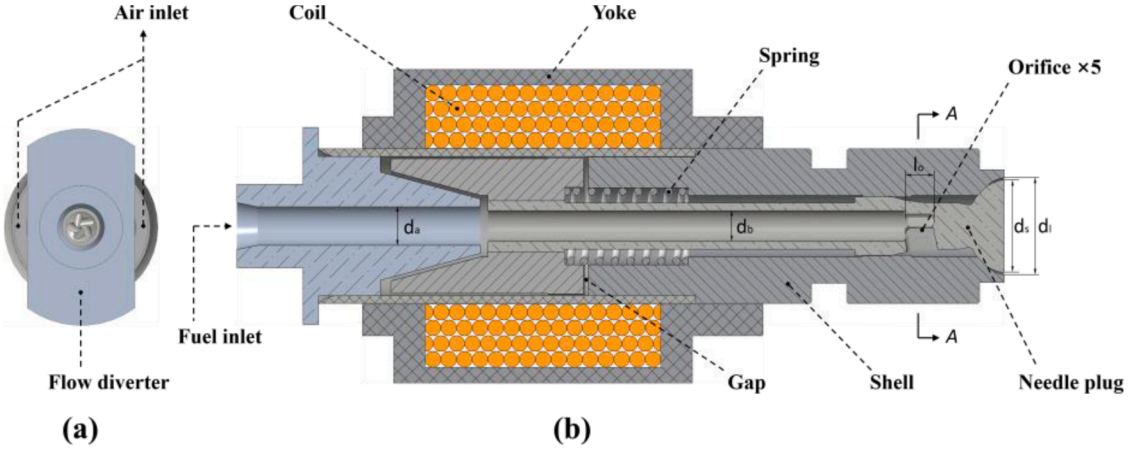

Fig. 1. Schematic of gas-liquid two-phase nozzle (a) side view and (b) section view. (d_a = 3.2 mm, d_b = 3.0 mm, l_o = 3.0 mm, d_s = 6.0 mm, d_l = 6.6 mm).

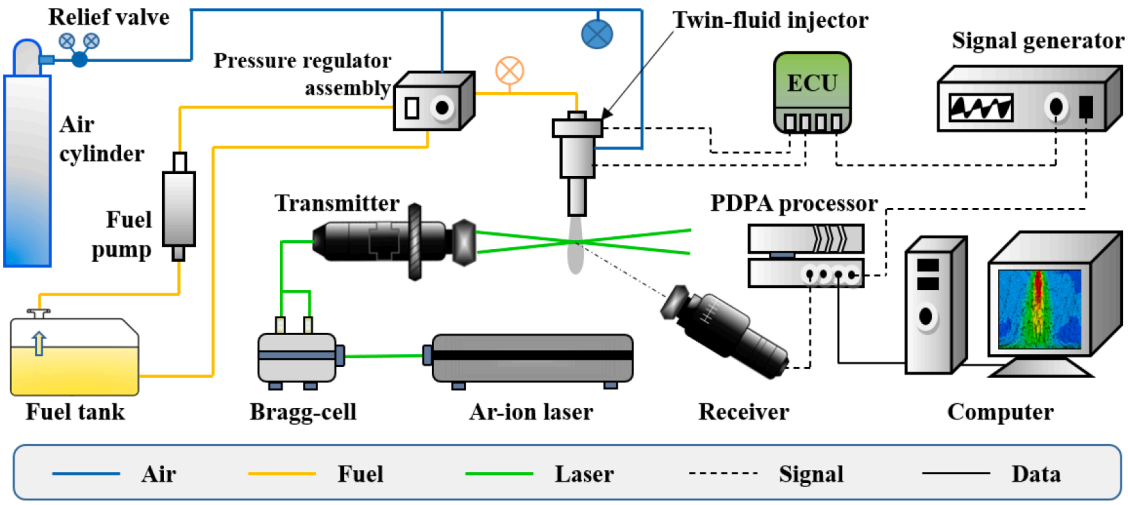

(a)

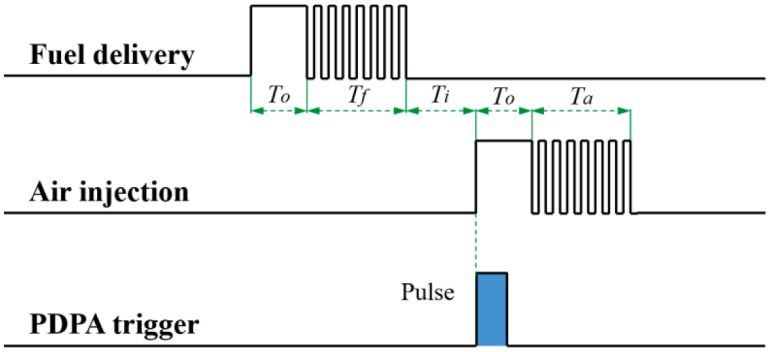

(b)

Fig. 2. (a) Schematic diagram of experimental system with PDPA configuration, (b) timing sequence of the injection driving pulse together with PDPA measurement. Both the events of fuel delivery and air injection are executed by a solenoid-driven nozzle with "peak-hold" current in which T_o represents the duration for nozzle to open, T_o and T_o denotes the duration to maintain opening status for fuel delivery and air injection, respectively.

number of previous investigations, it is relatively difficult to accurately describe the collision between the small droplets produced within the whole spray flow field because the number of droplets in the spray is so enormous that the collision between each other cannot be accurately determined. In the droplet dense region, collision may occur between droplets of various sizes, with a variety of collision parameters, at various spray positions and in multiple droplets successively colliding. Therefore, previous studies mainly adopted single droplet Weber number to estimate the collision Weber number (Saha et al., 2012). Most recently, the authors proposed a practical approach for collision Weber number estimation, influence of size ratio on collision dynamic was considered. However, influence of liquid mass loading ratio has not been concerned.

In the present study, we mainly focus on the atomization of internal-mixing twin-fluid jet implemented with intermittent injection, which has been rarely addressed in prior studies. The commonly designed annular nozzle was adopted together with the moderately complex upstream structure to generate the pulsed jet. The main objective of the present investigation is to address the gap in understanding the well-characterized, turbulent, droplet-laden two-phase jet through a comprehensive and systematic experimental investigation. The format of the present paper is as follows. In Section 2, the experimental setup will be specified, followed by the data processing methods and uncertainty analysis. The main results and discussion including quasi-steady state two-phase jet, droplet statistics, gas-liquid interactions, etc. will be elaborated on in Section 3. In Section 4, the main conclusions are summarized.

2. Experimental arrangement

2.1. Generation of gas-liquid two-phase jet

The experiments were conducted on a test bench under atmospheric environment and room temperature condition. The two-phase jet generation system with a separate fluid supply has been described in detail in our previous study (Wu et al., 2021a), and will not repeat in this paper Fig. 1 depicts a horizontal cross-sectional view of the gas-liquid two-phase nozzle, which employs a solenoid-driven reciprocating needle plug to implement a pulsed jet. The excitation coil is wound around the nozzle shell and wrapped by a magnetic yoke. Regardless of the coil, the nozzle is predominantly composed of a pair of precisely matched nozzle shell and needle plug. Nozzle shell head is designed with a hemispherical deletion, which can match well with the needle plug tip of a hemispherical entity. When the nozzle is open, an annular exit with diverging section is formed. The upstream of the needle plug is designed with a hollow tube and connected to the diverging exit through orifices. Gas flows via the flow channels on both sides of the diverter, while liquid flows through the center hole. When the nozzle is opened, an annular

exit with diverging section is first formed between the surface of the needle plug tip and the spherical surface of the shell head. Then the gas flow is established from the diverter's sides into the hollow tube of the needle plug, the orifices, and the annular diverging exit. Liquid enters the hollow tube of the needle plug through the center hole of the diverter and is injected under the entrainment of the airflow. The gas is maintained at a constant pressure of 700 kPa inside the nozzle and the liquid is supplied with a pressure of 800 kPa.

N-octane and compressed air were used as the liquid and gas phases, respectively. Unlike the continuous jets involved in most two-fluid jet issues, this study focuses on intermittent gas-liquid jets generated by a pulsed nozzle. The main operating parameter is the mass loading ratio (the ratio of liquid mass flow rate to the carrier phase mass flow rate) ϕ_m, which is defined as:

$$\phi_m = \dot{m}_l / \dot{m}_g \tag{2}$$

where $\dot{m}_l$ and $\dot{m}_g$ are the mass flow rate of liquid and gas respectively. Due to the intermittent and transient feature of pulsed jets, the mass flow is varied by altering different gas-liquid supply masses in a single jet to further quantitatively characterize the mass flow in this study. Previous research (Wu et al., 2021b) shows that the injected mass for gas phase is proportional to the opening time of the nozzle and the delivered liquid mass in a single jet can be regulated by the liquid injector within the system. In this study, the $\dot{m}_l$ ranges from 2.14 g/s to 11.44 g/s and the $\dot{m}_g$ is fixed at 3.54 g/s under the constant nozzle opening duration of 2.5 ms.

2.2. Visualization and measuring techniques

Fig. 2(a) shows the schematic diagram of experimental system. In this study, two conventional optical techniques were used to visualize and measure gas-liquid jets. Near-field jet was visualized by using backlight illumination imaging technique (i.e., shadowgraph). A high-speed camera (Phantom V7.3) was used to capture instantaneous jet morphology which was backlit illuminated by a diffused high-power LED light (i.e., PI-Luminor200, from Microvec Inc.). The camera was set at 10,000 frames per second (fps) with an exposure time of 50 μs, and a captured image resolution of 512 × 512 pixels. The corresponding physical image resolution was approximately 0.18 mm/pixel. More information can be found in our previous publication (Wu et al., 2020a).

A two-dimensional phase-Doppler particle analyzer (PDPA) from Dantec Dynamics Inc. was used to make simultaneous measurements of droplet size and velocity. The PDPA test system principally consists of a stand-alone Ar-ion laser, a Bragg cell, a transmitter, a receiver and a PDPA signal processor system. During the measurement, droplet diameter is determined in light of the difference in the phase shift between two Doppler burst signals emitted by the droplet passing through the measurement volume, whereas the droplet velocity is determined from the Doppler burst frequency (Kannaiyan and Sadr, 2014). The first-order refraction Doppler signal in forward-scatter mode is collected by the receiver and these signals are then processed by a processing unit to calculate the droplet size and velocity, which have been described by Albrecht et al. (2013) in more detail regarding the working principle and methodology of the PDA technique. In this experiment, a multiline Ar-ion laser produced a horizontally polarized light beam (0.8 W output power), which was split into four beams including two green ones (λ = 514.5 nm) and two blue ones (λ = 488 nm). Thereinto, the laser beam with the wavelength of 514.5 nm is used to measure the droplet axial velocity and diameter while the laser beam with the wavelength of 488 nm is used to measure the droplet's radial or tangential velocity. The laser beams were then transferred to the transmitter by optical fibers and symmetrically intersected by the transmitting lens with a focal length of 310 mm. The intersecting beams formed a prolate ellipsoidal measuring volume with an axis length of 76 × 76 × 630 μm. The receiver probe was positioned at an angle of 70° from the forward direction to collect the light scattered from droplets and to minimize reflections. The locating of the measurement volume in the actual spray will be described in the following text.

Table 1
Test conditions.

Case No.	$\dot{m}_l$ (g/s)	Φ_m	P_l (MPa)	P_g (MPa)	Sampling location (mm)	
					x	r
1	2.14	0.60	0.8	0.7	50	0
2	3.23	0.91	0.8	0.7	50	0
3	5.18	1.46	0.8	0.7	30	0
4	5.18	1.46	0.8	0.7	40	0
5	5.18	1.46	0.8	0.7	50	0
6	5.18	1.46	0.8	0.7	50	2
7	5.18	1.46	0.8	0.7	50	4
8	5.18	1.46	0.8	0.7	50	6
9	5.18	1.46	0.8	0.7	50	8
10	5.18	1.46	0.8	0.7	50	10
11	5.18	1.46	0.8	0.7	60	0
12	7.26	2.05	0.8	0.7	50	0
13	9.35	2.64	0.8	0.7	50	0
14	11.44	3.23	0.8	0.7	50	0

Table 2
Uncertainties of D_{32} and D_{90} from PDPA measurements.

Case No.	Φ_m	Uncertainties (dimensionless)	
		D_{32}	D_{90}
1	0.60	±0.0461	±0.0389
2	0.91	±0.0379	±0.0328
3	1.46	±0.0245	±0.0145
4	1.46	±0.0297	±0.0198
5	1.46	±0.0321	±0.0236
6	1.46	±0.0337	±0.0221
7	1.46	±0.0384	±0.0258
8	1.46	±0.0401	±0.0294
9	1.46	±0.0445	±0.0323
10	1.46	±0.0477	±0.0363
11	1.46	±0.0364	±0.0270
12	2.05	±0.0314	±0.0225
13	2.64	±0.0303	±0.0211
14	3.23	±0.0288	±0.0204

A self-developed Electronic Control Unit (ECU) was used to output the drive signal of the injection system and the trigger signal for the high-speed camera and PDPA. The timing sequence of the injection driving pulse together with PDPA measurement is shown in Fig. 2(b). The laptop can modify the control signal in real time and monitor the working status of the injector at the same time. A computer is used to display the spray morphological evolution and store the spray raw image of different working conditions. To eliminate the influence of the last spray, the injection frequency in actual test was less than 0.1 Hz. The test conditions are listed in Table 1.

2.3. Data processing and uncertainty

An in-house Matlab program was used to process the jet raw images captured by the high-speed camera to obtain the time-resolved jet macroscopic morphology. The program included image background subtraction, contrast adjustment, pixel value filtering, and binarization (Gao et al., 2019). The droplets captured by PDPA were statistically calculated to obtain the droplet diameter distribution. Meanwhile, the droplet arithmetic mean diameter D_{10} and Sauter mean diameter D_{32} (typically defined by $D_{32} = \sum N_i D_i^3 / \sum N_i D_i^2$, where N_i is the number of droplets within the corresponding droplet size scale, while D_i is the droplet diameter for each trapped droplet) were used to characterize the average droplet size. Furthermore, the droplet representative diameter of D_{max} (denotes the droplet diameter at which 90% of the total liquid volume is in droplets of smaller diameter) was used to evaluate the maximum droplet size. Repeated measurements were taken at all operating conditions and the dimensionless uncertainty U_{se} of the

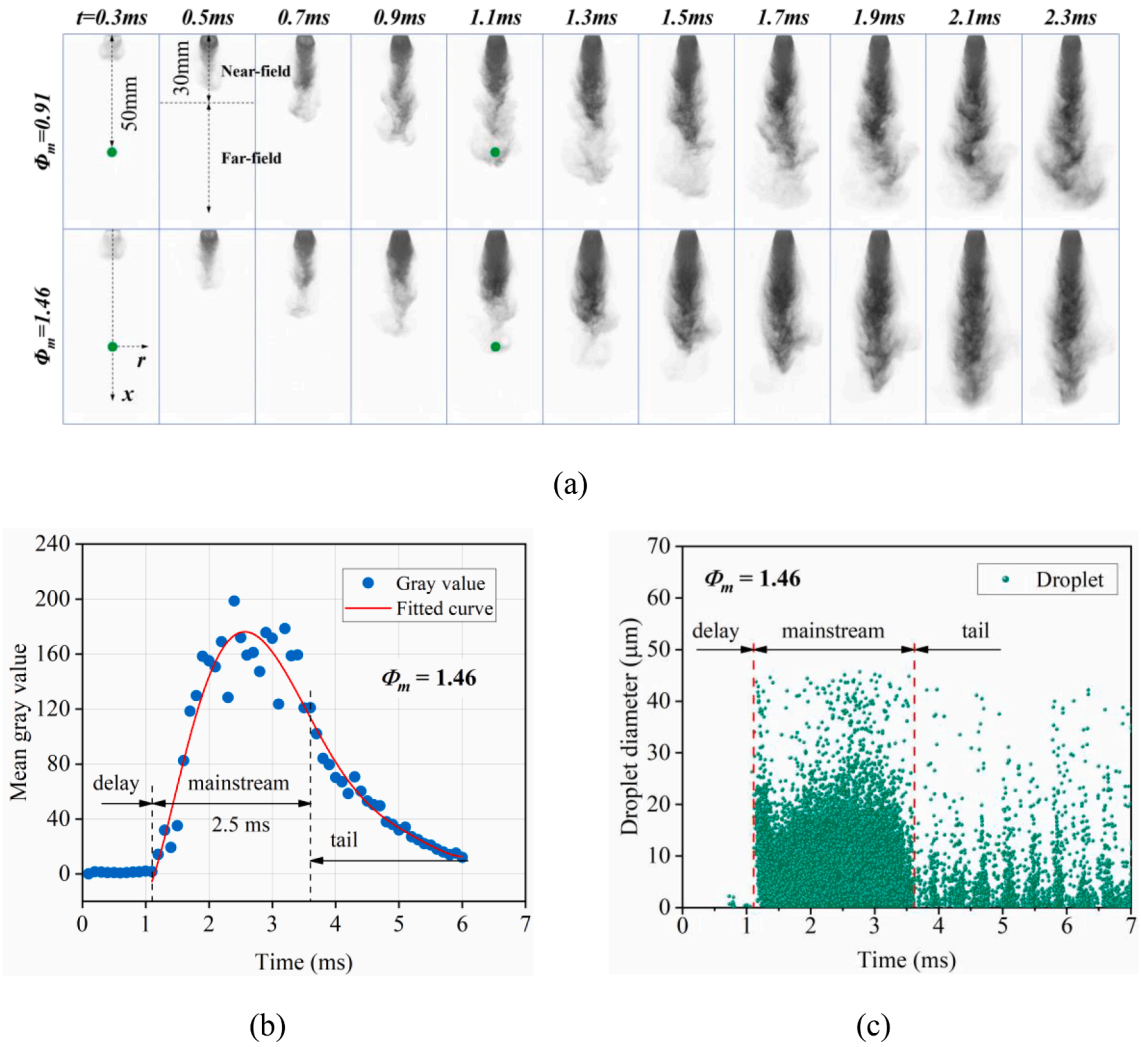

Fig. 3. (a) Time-resolved evolution of pulsed gas-liquid two-phase jet at $\phi_m = 0.91$ and $\phi_m = 1.46$, (b) mean gray value at the location of PDPA measurement volume and (c) PDPA data for droplet diameter at the sampling location of $x = 50$ mm. Near-felid is defined as $x \leq 30$ mm while far-felid is denoted by $x > 30$ mm.

obtained data was calculated based on the standard error, as follows

$$U_{se} = \pm\sqrt{\frac{\sum_{i=1}^{N}(\alpha_i - \overline{\alpha})^2}{N \times (N-1)\cdot\overline{\alpha}^2}} \tag{3}$$

where N is the measurement time and α_i is the measured value for each time. $\overline{\alpha} = \sum_{i=1}^{N}\alpha_i/N$ represents the arithmetic mean value of multiple measurements Table 2. presents the uncertainties of D_{32} and D_{max} from PDPA measurements for all the cases. One can see that mass loading ratio, axial and radial sampling locations have a certain influence on the uncertainty results, which is principally attributed to the data sampled under different conditions (Doudou, 2005). It is apparent that the maximum dimensionless uncertainty error of this study does not exceed 5%, which verifies the reliability and reproducibility of the test results within a certain range.

3. Results and discussion

3.1. Quasi-steady state jet and droplet statistics

Previous studies (Lasheras et al., 1998; Mlkvik et al., 2015; Urbán et al., 2017; Varga et al., 2003; Zaremba et al., 2017) on twin-fluid jets or gas-liquid two-phase sprays mainly focused on the continuous jets under steady-state flow conditions. However, the pulsed jet has been barely concerned. In contrast, pulsed jets are characterized by significant transient jet establishment and dissolution stages. Consequently, this study highlights the investigation concerning the gas-liquid two-phase jet generated by a pulsed twin-fluid atomizer. Time-varying morphological evolutions of the single jets for $\phi_m = 0.91$ and $\phi_m = 1.46$ conditions are shown in Fig. 3(a). The position of the PDPA measuring volume, which is located at $x = 50$ mm, is selected and marked (green dots). The raw images (RGB type) of the jet recorded by high-speed camera are consistently processed into grayscale images and arranged in a sequence every 0.2 ms. Comparison of the two jet sequences reveals that there is no significant difference between two jet morphologies, however, higher ϕ_m produces significantly darker color of the jet morphology, specifically in the jet far-field, indicating more liquid fuel was injected.

The grayscale values of the jet image sequence at $x = 50$ mm below the nozzle exit were extracted sequentially for the case of $\phi_m = 1.46$, and the variation of the mean grayscale value versus the injection time t was obtained, as shown in Fig. 3(b). It can be found that the spray tip has not yet reached the PDPA measurement volume and the mean gray value is 0 for $t \leq 1.1$ ms, beyond which jet starts to pass through the PDPA measuring volume continuously hence the mean gray value gradually increases to the maximum level. Subsequently, the mean gray value diminishes to 0 as t further develops. Time period for $t \leq 1.1$ ms can be defined as detection delay period, during which the jet is generated but the tip of jet head has not reached the PDPA measurement volume, and

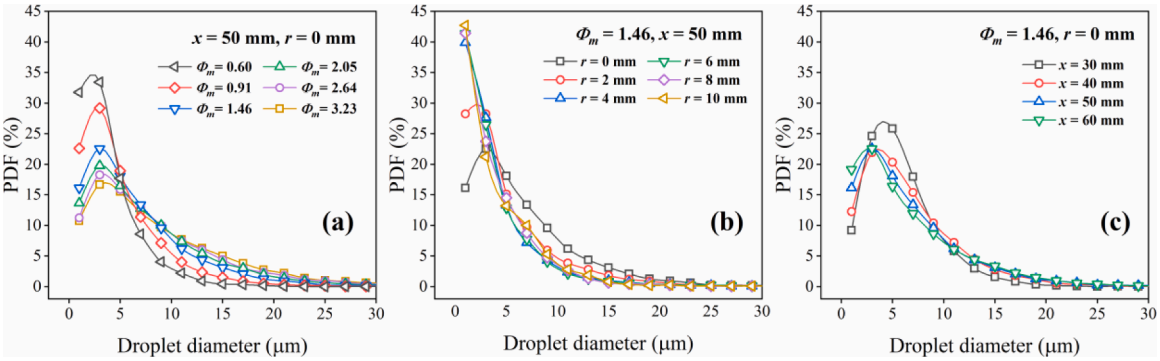

Fig. 4. Measured PDF of droplet diameter at (a) various ϕ_m conditions at $x = 50$ mm and $r = 0$ mm, (b) various radial locations under $\phi_m = 1.46$ and $x = 50$ mm; (c) various axial distances under $\phi_m = 1.46$ and $r = 0$ mm.

no individual droplets can be detected. This is followed by the mainstream period ($1.1 < t < 3.6$ ms), during which jet keeps on evolving and passes across the measurement volume so that sufficient droplets are captured, as seen in Fig. 3(c). Note that this stage lasts for 2.5 ms, which corresponds to the actual nozzle opening duration. After mainstream, the nozzle is closed hence jet loses its source of momentum and gradually vanishes. Since sufficient droplets can be captured in the jet mainstream period, which is regarded as an approximately transient quasi-steady jet therefore the detection delay and jet tail were ignored in this study. Droplets captured in the mainstream period were employed for the analysis of the following sections.

For combustion systems, an accurate depiction of the droplet size distribution is essential for further analysis of phase changes, heat transfer, evaporation rates, and the quality of combustible mixture formation (Williams, 2018). In this study, PDF (Probability Density Function) of discrete droplet diameter captured by PDPA was selected for droplet size distribution, as shown in Fig. 4. The PDF was profiled with a dotted line graph as a function of droplet diameter with the interval of 3.0 μm chosen to be large enough to contain adequate droplets yet small enough to obtain more details Fig. 4.(a) shows the measured size PDFs of droplets from different ϕ_m cases. It can be found that when ϕ_m is small, the distribution of droplet diameter shows a rather pronounced monodisperse characteristic, i.e., droplet diameter is uniformly dispersed in a small-scale range (about 0-5 μm). With the increase of ϕ_m, droplet diameter tends to be polydisperse, leading to the appearance of larger diameter droplets Fig. 4(b) and Fig. 4(c) show the droplet diameter distributions at different radial and axial positions for the case of $\phi_m = 1.46$, respectively. One can see that the proportion of small diameter droplets gradually increases as the sampling position gradually moves away from the jet axis. The distribution of droplet diameters

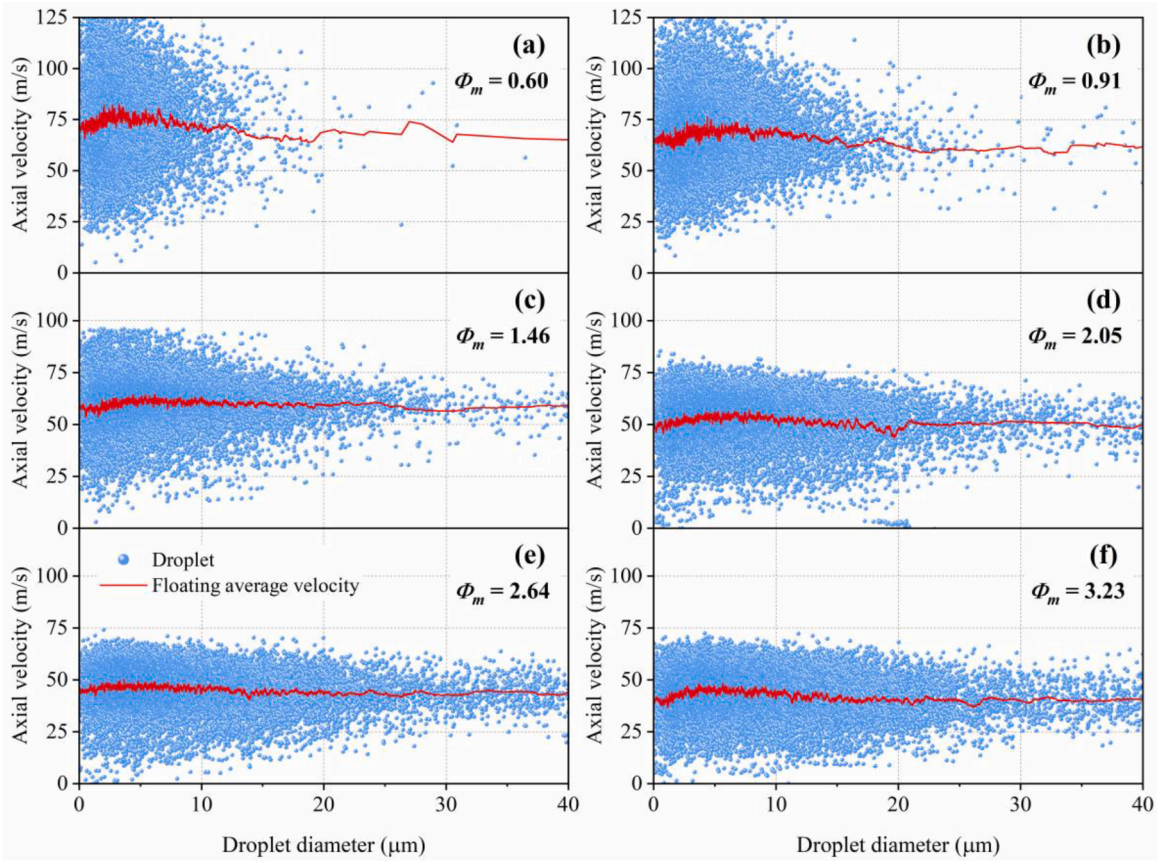

Fig. 5. Typical correlation between droplet diameter and axial velocity with floating average velocity (red line) for different ϕ_m cases at $x = 50$ mm, $r = 0$ mm.

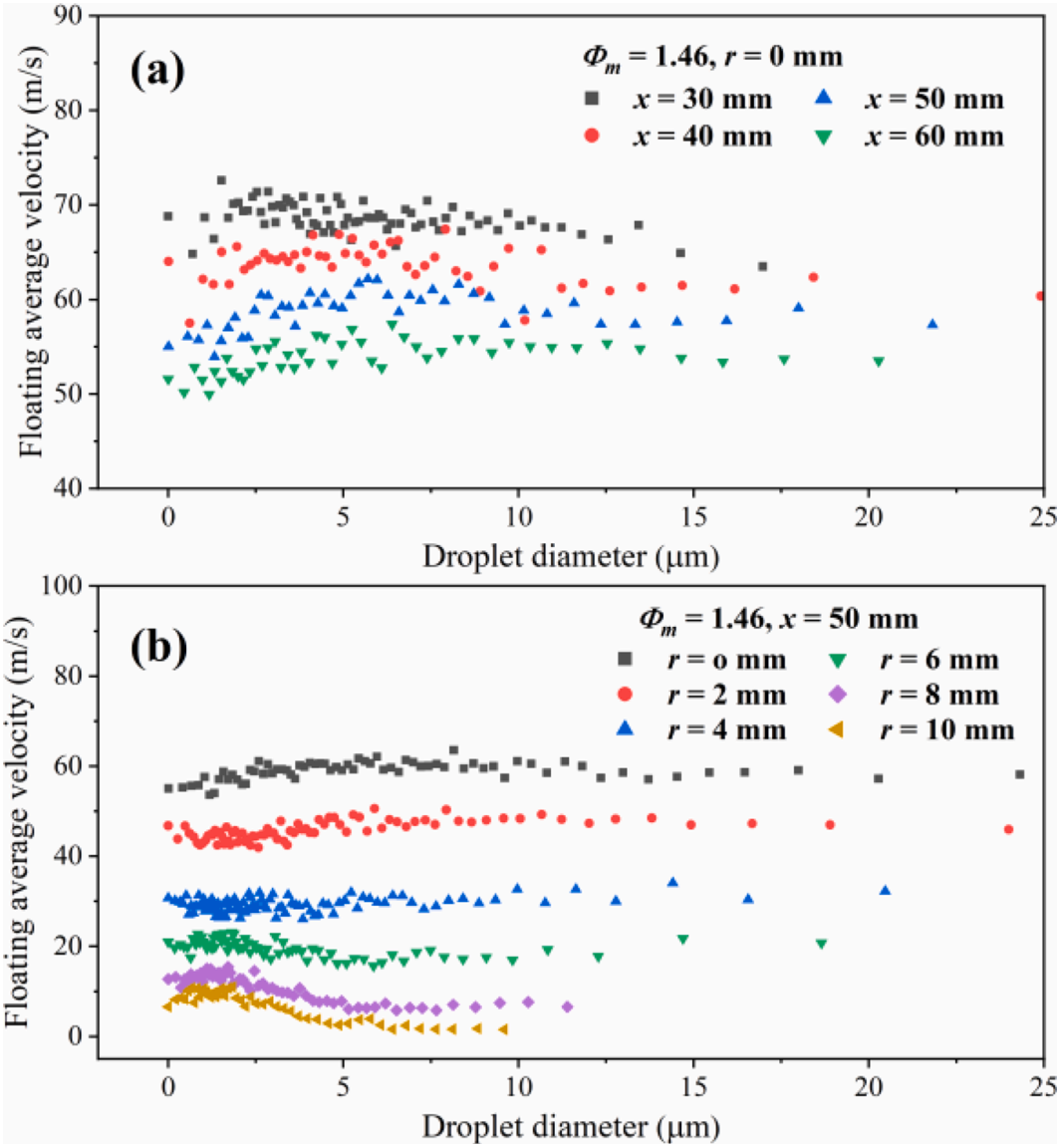

Fig. 6. Floating average profiles of axial velocity for (a) $\phi_m = 1.46$, $r = 0$ mm and (b) $\phi_m = 1.46$, $x = 50$ mm.

along the jet axis does not vary enough to be distinguishable in the selected axial sampling range.

3.2. Droplets size-velocity distribution and correlation analysis

For gas-liquid two-phase jets, there exists momentum transfer between gas and liquid phases during not only the internal mixing process but also the external jet formation and evolution (Jiang et al., 2010). The relative velocity between gas and liquid phases (a.k.a. the slip velocity) plays an essential role in liquid phase disintegration and subsequent droplet breakup (Lasheras et al., 1998). Moreover, droplets of different size classes in a gas-liquid two-phase jet may exhibit different velocities of motion according to Zaremba et al. (2017). A fact that cannot be ignored is that discrete droplets tend to travel with external high-speed gas flow. Smaller droplets (characterized by relatively lower Stokes number, as elaborated in Section 3.3) are more likely to flow with the gas-phase flow therefore produces smaller gas-liquid shear velocity hence smaller interface instability, while larger droplets with higher inertia result in the large gas-liquid relative velocity hence more significant interface instability.

Fig. 5 statistically shows the scatter plots of droplet axial velocity versus diameter distributions for different ϕ_m cases. According to Zaremba et al. (2017), a typical correlation between droplet size and velocity can be expressed with a floating average velocity V_f for a certain droplet diameter scale D_i, as

$$V_f = \frac{1}{n}\left(\sum_{i-n/2}^{i+n/2} V_i\right) \tag{4}$$

where i denotes the i^{th} droplet (with the size of D_i and velocity of V_i) arranged in increasing order of size and n is fixed to 100. The floating average velocity is plotted with a red solid line.

It can be seen that velocity range of the sampled droplets decreases with the increase of ϕ_m, while the scattering range of the diameter is promoted by the increase of ϕ_m, which is consistent with the previous statistical results on the droplet diameter PDF, as shown in Fig. 4(a). For $\phi_m = 0.60$, the floating average velocity presents a moderate tendency to first increase and then decrease when droplet diameter is less than 10 μm. This is due to the fact that the decrease of ϕ_m leads to an increase in gas velocity since the momentum transfer between gas and liquid phase is diminished (Wu et al., 2020b). In this situation, the region where the droplets are accelerated (i.e., negative slip velocity, as described below)

Table 3
Pearson's correlation coefficient $|C_{dv}|$ for partial test conditions.

Conditions		Droplet size range (μm)				
Φ_m	x/r (mm)	$0 \le D \le 10$	$10 \le D \le 20$	$20 \le D \le 30$	$30 \le D \le 40$	$0 \le D \le 40$
0.60	50/0	0.0348	0.1406	0.1067	0.0141	0.0034
0.91	50/0	0.0902	0.1707	0.1170	0.0675	0.0021
1.46	50/0	0.1087	0.0460	0.0546	0.0862	0.0312
2.05	50/0	0.1072	0.1066	0.0289	0.1310	0.0334
2.64	50/0	0.0128	0.0560	0.0010	0.0070	0.0886
3.23	50/0	0.0748	0.0819	0.0112	0.0006	0.0953
1.46	30/0	0.0378	0.1151	0.0511	0.1434	0.0665
1.46	50/10	0.2921	0.1715	0.1487	0.1742	0.1506

by the gas will extend further downstream of the jet. Thus, small-sized droplets will be continuously accelerated, while this observation becomes progressively less pronounced for large-size droplets due to their inferior property in accompanying gas-phase flow. Similar results also can be observed for $\phi_m = 0.91$, beyond which floating average velocity tends to be flatter and independent of droplet diameter. This indicates that the droplet mean velocity is more consistent for different diameter ranges. Additionally, this observation demonstrates that at this sampling location ($x = 50$ mm, $r = 0$ mm), droplets with different sizes have already reached the gas velocity and are accompanied by the local gas-phase flow. In light of the results for different ϕ_m conditions, it can be found that droplet size-velocity distribution is inconsistent with that from Zaremba et al. (2017), probably due to Zaremba et al.'s experiments mainly focus on the relatively higher ϕ_m (denotes quite smaller gas-phase mass flow rate) than our experiments.

Axial and radial profiles of floating average velocity versus droplet diameter are presented in Fig. 6. As the axial distance increases, the floating average velocity first decreases then moderately increases with droplet size increasing. This indicates that at the positions close to the nozzle, smaller droplets tend to move with a higher velocity and the larger droplets with a smaller velocity. At positions far from the nozzle, and vice versa. However, the floating average velocity for various radial locations shows an approximately flat trend with droplet diameter for $r < 6$ mm, since these sampling locations are close to jet axis and the local gas-phase flow velocity is relatively large. For $r = 8$ mm and $r = 10$ mm, it is apparent that the floating velocity shows a general decreasing function as droplet diameter, which is due to the restricted acceleration of large-size droplets at the periphery of the jet.

Li et al. (2013) stated that PDPA is a non-intrusive means of measuring droplet diameter and velocity information simultaneously, therefore the correlation coefficient can be used to quantify the relationship that may exist between sampled droplet diameter and velocity under different operation conditions. In this study, five size ranges were divided according to droplet diameter, and the Person correlation coefficient C_{dv} is calculated to quantitatively characterize the local as well as the global droplet diameter-velocity correlation, as follows (Warner, 2012)

$$C_{dv} = \sum (D_i - \overline{D})(V_i - \overline{V}) \Big/ \sqrt{\sum (D_i - \overline{D})^2 (V_i - \overline{V})^2} \tag{5}$$

where D_i and V_i are the diameter and velocity of the ith droplet, respectively. $\overline{D}$ and $\overline{V}$ are the arithmetic mean values of the sampled droplet diameter and velocity, respectively Table 3. shows the obtained Pearson correlation coefficients for selected conditions, where the first

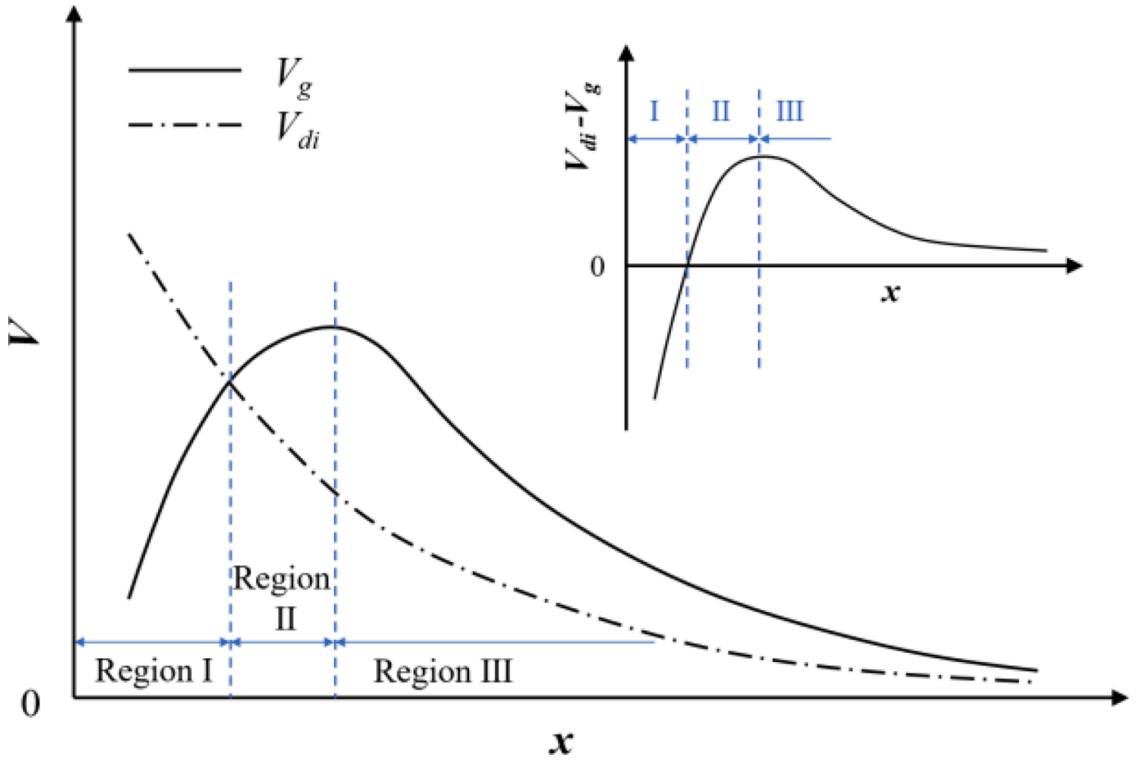

Fig. 7. Region diagram of downstream evolution of mean slip velocity between liquid (droplets) phase and local gas-phase (air). Region I: droplet acceleration; Region II: velocity overshooting; Region III: droplet deceleration.

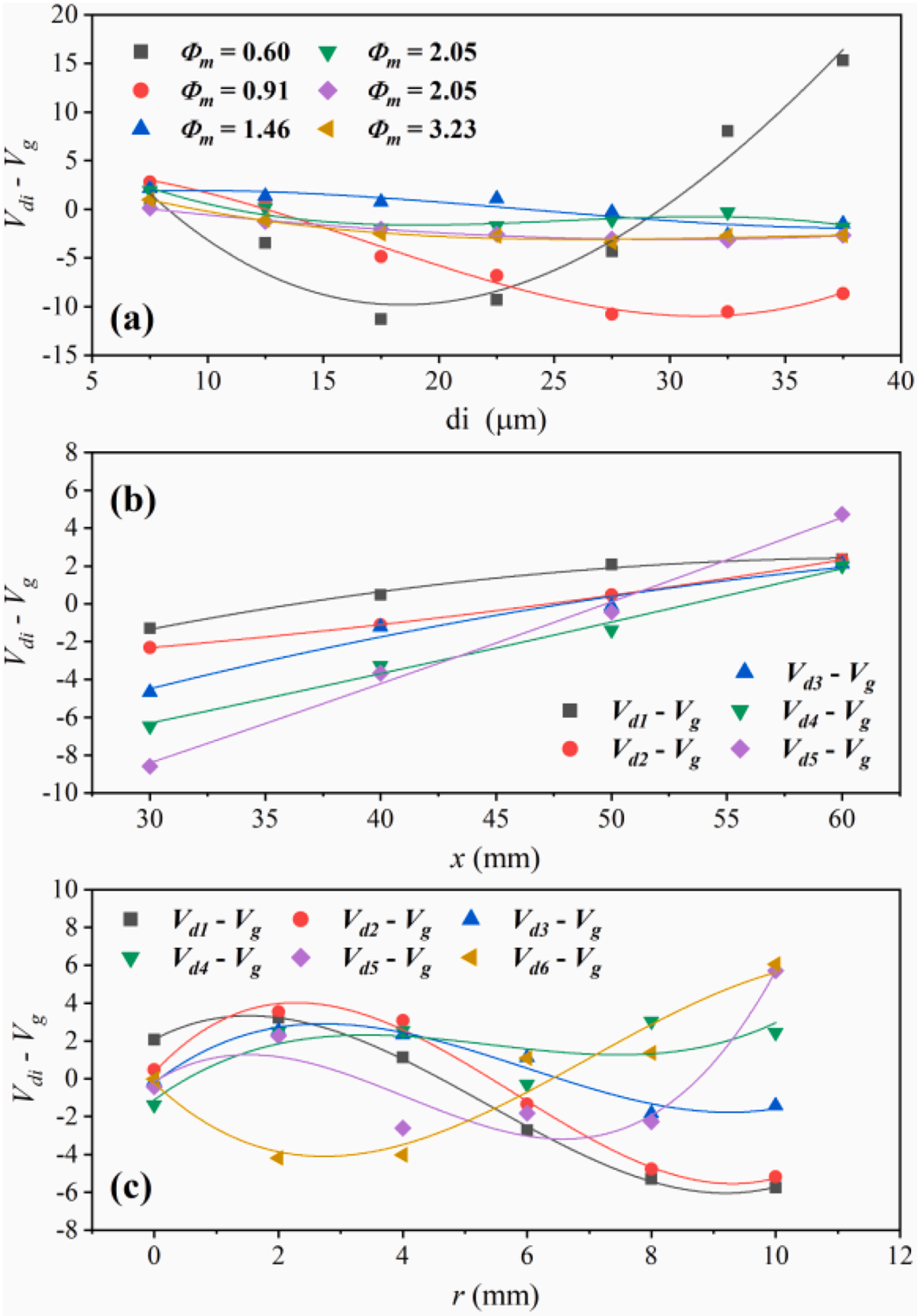

Fig. 8. Mean slip velocity ($V_{di} - V_g$) between the droplets and the surrounding gas measured at the jet centerline under (a) various ϕ_m cases, (b) various axial positions x and (c) various radial positions r. Note that the droplets have been classified in five size bins, d_1 denotes the diameter between 5 and 10 μm; d_2 the diameter between 10 and 15 μm; d_3 the diameter between 15 and 20 μm; d_4 the diameter between 20 and 25 μm; d_5 the diameter between 25 and 30 μm. The gas velocity has been measured by the droplets in the size bin with diameter less than 5 μm.

four groups represent the local C_{dv} while the last group represents the overall C_{dv}. The values of Person correlation coefficient range from $0 < |C_{dv}| < 1$, indicating the degree of correlation. $|C_{dv}| < 0.3$ indicates that there is no correlation between the two variables. The data in Table 3 suggest that $|C_{dv}|$ for all droplet size ranges do not exceed 0.3, proving that there is no noticeable correlation between the atomized droplet diameter and velocity for this jet at the selected operating conditions, which is also close to the results of Li et al (2013).

The relative velocity between droplet and carrier (gas-phase) can be quantitatively described and compared using the mean slip velocity

$V_{di} - V_g$ (Lasheras et al., 1998), where *di* denotes the size bins every 10 μm starting from 5 μm of the droplet diameter. Droplets with diameters smaller than 5 are used to measure the gas velocity, which will be elaborated in following Section 3.3. The downstream evolution of mean droplet velocity can be divided into three regions based on mean slip velocity, i.e., acceleration (I), velocity overshooting (II), and deceleration (III) based on the analysis of Lasheras et al. (1998), see Fig. 7. Droplet is continuously accelerated in region I, then exceeds the gas velocity in region II and finally reaches the maximum slip velocity. Subsequently, droplet velocity gradually decreases to the local gas velocity in region III. Note that droplets remain accelerated by the carrier in the first two regions Fig. 8(a) shows the mean slip velocity under various ϕ_m cases. It is seen that $V_{di} - V_g$ is close to 0 when ϕ_m is greater than 1.46, indicates the measurement location with $x = 50$ mm, $r = 0$ mm is already located in region III for all these cases. When ϕ_m is degenerated to 0.91, a negative slip velocity is found for small droplets, which is more pronounced for the case of $\phi_m = 0.60$. This is because a smaller mass loading ratio leads to an increase in gas velocity, which in turn causes the droplets to take longer time to be accelerated. Therefore, it is reasonable to estimate that the boundary line between different regions in Fig. 7 will right shift along the x direction as ϕ_m increases Fig. 8(b) and Fig. 8(c) depict the mean slip velocity of various axial and radial positions under $\phi_m = 1.46$, respectively. The mean slip velocity shows an increasing function of x, and this tendency becomes more noticeable as the droplet size bin increases. When x is less than 50 mm, $V_{di} - V_g$ is almost negative, suggesting that the droplets of all sizes are keeping accelerated at this condition. After 50 mm, droplet starts to exceed the local gas-phase velocity, indicates that the boundary of regions I and II under this condition should be in the vicinity of $x = 50$ mm. For small-sized droplets from various radial positions, the mean slip velocity is positive for droplets close to the jet axis and negative for droplets far from the jet axis, which however gradually transitions to the opposite situation as the size bin increases, as shown in Fig. 8(c). This can be attributed to the fact that droplets at the jet axis are accelerated more rapidly to cross the aforementioned regions, while local gas velocity at the periphery of the jet will be significantly reduced by the aerodynamic resistance of the stagnant ambient atmosphere, which in turn weakens the acceleration effect on droplets.

3.3. Droplet Stokes number and local gas-phase flow

In the study of gas-liquid two-phase jet, especially droplet-laden jet in which discrete droplets are dispersed in the gas stream, the velocity characterization of the carrier-phase is essential for further understanding of droplet secondary breakup, droplet-turbulent interactions, and droplet-gas correlations (Balachandar and Eaton, 2009; Crowe et al., 2011). However, synchronous measuring of the carrier-phase and the dispersed-phase velocity still poses an immense challenge for the existing optical diagnostics. A common solution for PDPA measurements is to characterize the local gas flow velocity by using the velocity of small-size (typically less than 5 μm) droplets and the followability of these droplets for carrier flow velocity characterization is widely recognized and applied in previous studies (Ferrand et al., 2001; Ferrand et al., 2003; Jedelsky et al., 2018; Lasheras et al., 1998; Prevost et al., 1996; Wu et al., 2021b). In this study, we still made a followability evaluation of droplets ($D < 5$ μm) by considering the possible specificity of the problem we are concerning. The detailed validation and characterization of local gas-phase flow velocity are as follows.

For droplet-laden jet, interaction intensity between droplet and the surrounding gas can be explained by Stokes number *Stk*, a dimensionless criterion established to describe the behavior of droplets suspended in the carrier fluid (Feng et al., 2019; Jebakumar and Abraham, 2016). A droplet with a low *Stk* tends to follow external flow streamlines and therefore present perfect advection, while droplet motion with a large *Stk* is dominated by its inertia and continues along its original trajectory

Table 4
Characteristic parameters of gas-liquid two-phase jet.

	0.60	0.91	1.46	2.05	2.64	3.23
$R_{1/2}$ (mm)	10.01	10.45	11.82	14.36	15.72	16.01
V_{rms} (m/s)	26.55	21.34	12.75	11.52	10.99	11.47
τ_f (ms)	0.377	0.489	0.927	1.246	1.430	1.396
V_g (m/s)	80.67	70.35	59.79	53.02	47.37	44.78
Stk ($D = 5$ μm)	0.153	0.117	0.062	0.046	0.040	0.041
Stk ($D = D_{10}$)	0.085	0.116	0.123	0.122	0.133	0.154
Stk ($D = D_{32}$)	0.498	0.791	0.737	0.754	0.818	0.865
Re_g	57685	52519	50486	54386	53200	51217
Wes ($D = D_{32}$)	0.314	0.003	0.017	0.145	0.181	0.045
Wes ($D = D_{max}$)	1.269	0.010	0.041	0.296	0.336	0.082
Wet ($D = D_{max}$)	1.525	1.104	0.396	0.324	0.299	0.323

(Wu et al., 2021b). The *Stk* is normally defined as the ratio of the droplet response time τ_d to the flow response time τ_f, i.e.

$$Stk = \frac{\tau_d}{\tau_f} \tag{6}$$

For a spherical droplet, droplet response time can be taken as the time constant of the droplet in Stokes flow by

$$\tau_d = \frac{\rho_l D^2}{18\mu_g} \tag{7}$$

where D is the droplet diameter, ρ_l and μ_g represent the density of liquid droplet and dynamic viscosity of air, respectively. The flow response time can be obtained from a characteristic length scale and a velocity scale of the flow. In this study, τ_f is chosen as the ratio of a large eddy length scale $R_{1/2}$ (the half width of the spray jet, selected from mean velocity profile and for a conservative estimate here) to the standard deviation of carrier-phase fluctuating velocity V_{rms} (Ferrand et al., 2003; Manish and Sahu, 2019; Pope, 2000). The droplets with diameter less than 5 μm were selected as "tracer droplets" and temporarily assumed to follow the gas-phase flow almost completely to ascertain instantaneous local gas flow velocity (Crowe et al., 2011; Lasheras et al., 1998; Manish and Sahu, 2019; Wu et al., 2021a, b). Thus, the fluctuating velocity can be calculated as

$$V_{rms} = \sqrt{\langle v_g v_g \rangle} \tag{8}$$

where v_g is the fluctuating velocity of carrier-phase calculated by tracer droplets. The above parameters are evaluated separately for different ϕ_m cases, as listed in Table 4. To ascertain the effect of tracer droplet size on the difference in droplet response to the carrier fluid, five sets of tracer droplet size ranges below 5 μm were selected to calculate local gas-phase flow velocities by $V_g = \sqrt{\langle V_i V_i \rangle}$. The obtained local gas-phase velocity under various tracer droplet diameter ranges is shown in Fig. 9. It can be found that the diameter range has a negligible effect on the calculated local gas-phase flow velocity for the same ϕ_m case and the variation of V_g with ϕ_m approximately satisfies a quadratic function in the selected ϕ_m range, as seen in Fig. 9. The calculated V_g gradually decreases from 78 m/s to 44 m/s with the increase of ϕ_m in a certain range. To ensure that the samples are adequate and not affected by individual droplets, 0-5 μm was adopted as the size range of tracer droplets in this study.

Fig. 10 shows the range of *Stk* of 10,000 sample droplets from different ϕ_m cases by displaying the magnitude of *Stk* with different colors in a three-dimensional scatter plot. When using small droplets to characterize the local gas-phase flow, it is generally considered that the smaller droplet *Stk* provides a higher tracking accuracy. Generally, droplets with $Stk \ll 1$ follow the gas flow faithfully. If $Stk < 0.1$, It can be considered the error of tracking accuracy is less than 1% Crowe et al., 2011; Tropea and Yarin, 2007). It is clear that the *Stk* of the tracer droplets does not exceed 1 for all ϕ_m cases and some cases are merely just over 0.1, as seen in Table 4. Therefore, we confirm the tracking accuracy

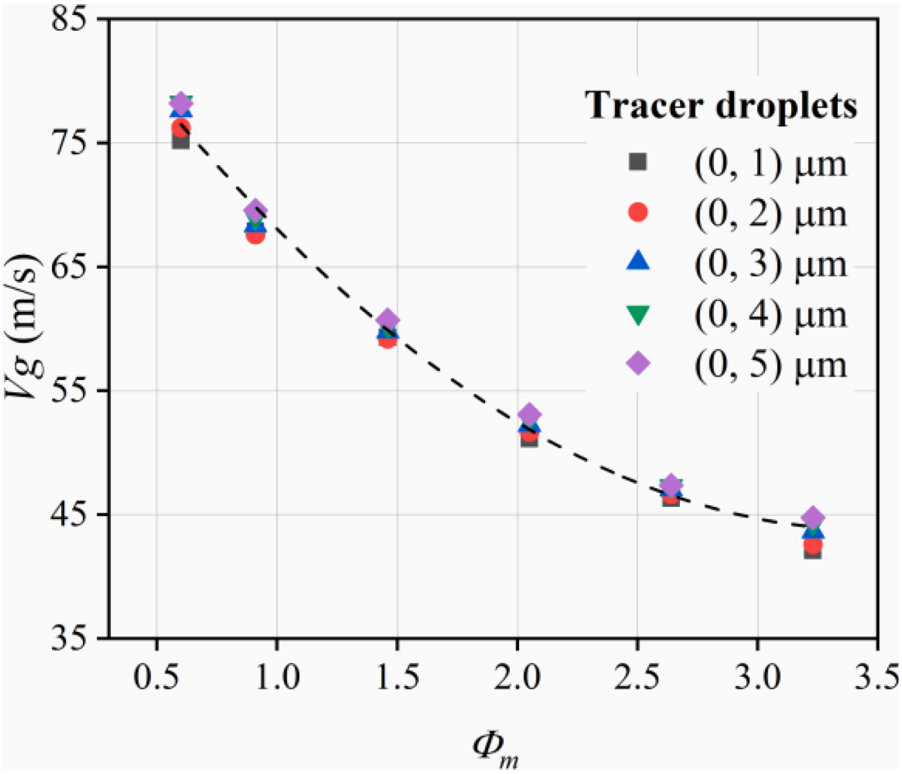

Fig. 9. Local gas velocity estimated by the selecting tracer droplets of different diameter ranges.

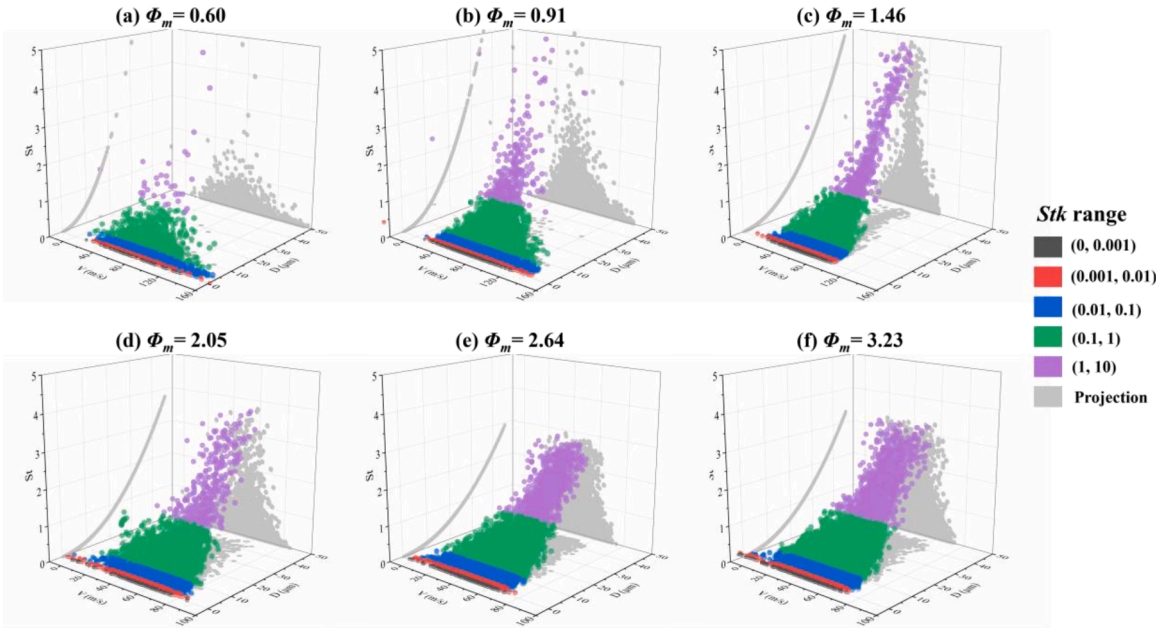

Fig. 10. Scatter plot of droplet ***Stk*** distribution with data range. Only 10000 samples are shown for better visibility under various ϕ_m cases.

error of adopting tracer droplets to characterize the local gas flow velocity is less than 1% and the above-mentioned assumption is justified. A noteworthy observation is that the projection of the scatter plot of the *Stk* distribution in the X-Z plane appears as a curve. This can be explained by the fact that when using Eq. (6) and (7), as well as the method of tracer droplet to characterize the local gas velocity, the obtained *Stk* by simplification is quadratically related to D_i, independent of V_i. The Reynolds number (Re_g) of the local gas flow can be calculated based on the obtained V_g and half-width of the jet (large eddy length scale $R_{1/2}$), given by $Re_g = \rho_g V_g R_{1/2}/\mu_g$ (Manish and Sahu, 2019). The calculated Re_g for various ϕ_m cases can be seen in Table 4. Due to the simultaneous influence of V_g and $R_{1/2}$ in the numerator, Re_g is generally stabilized in the order of 10^4-10^5, indicating the gas-phase flow possesses high-intensity turbulence characteristics.

3.4. Droplet Weber number and breakup estimation

Discrete droplets are usually subjected to break up under the stress of

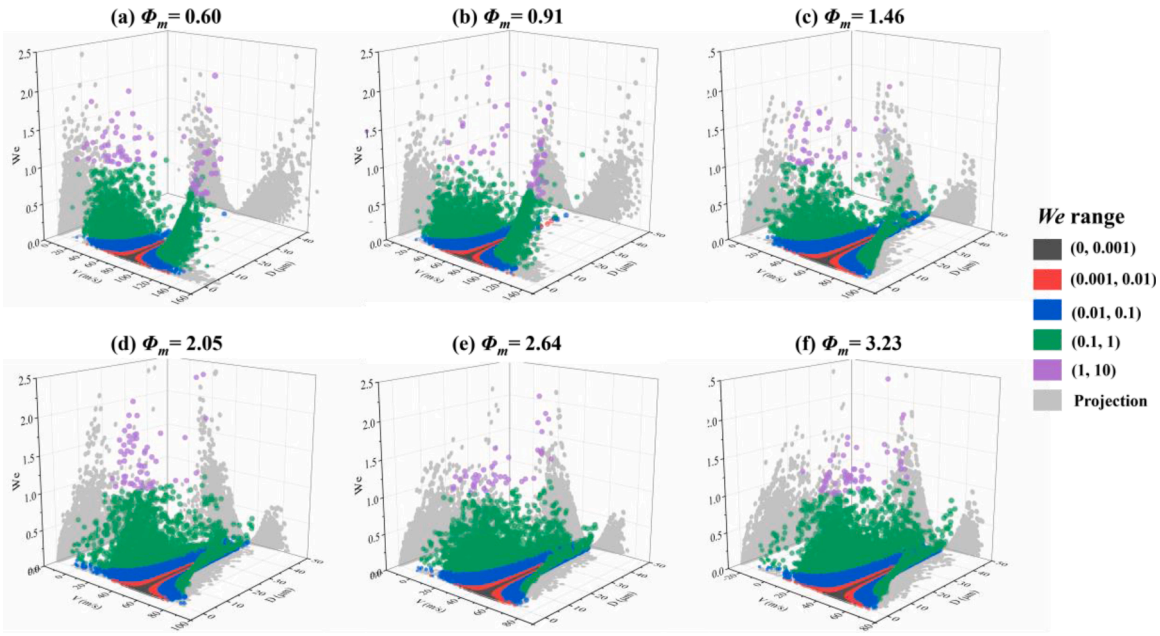

Fig. 11. Scatter plot of droplet *Wes* distribution with data range. Only 10000 samples are shown for better visibility under various ϕ_m cases.

the surrounding gas turbulence (Guildenbecher et al., 2009). Following the classical decomposition of turbulent motion into a mean and a fluctuating component, the forces acting on the liquid droplets can be expressed as the sum of the force generated by the mean relative velocity between droplet and gas (i.e., slip velocity) and the force resulting from the turbulence fluctuations (Lasheras and Hopfinger, 2000). Therefore, droplet breakup caused by these two forces is usually distinguished as shear breakup and turbulent breakup.

Previous studies suggest that droplet breakup occurs when the shear Weber number *Wes* of a droplet exceeds a critical value of Wes_c, given by

$$Wes = \frac{\rho_g \left(V_i - V_g\right)^2 D_i}{\sigma} > Wes_c \tag{9}$$

where σ represents the liquid surface tension Hinze's (1955). investigation of water droplets reveals that the order of Wes_c is close to 10, and this critical value increases with liquid viscosity increasing (Pilch and Erdman, 1987). The *Wes* of droplet is graphed in a three-dimensional scatter plot with velocity as the X-axis and diameter as the Y-axis for all ϕ_m cases, as shown in Fig. 11. Likewise, the value range of *Wes* is divided using scatter of different colors. The calculated *Wes* using D_{32} and D_{max} can be seen in Table 4. Obviously, *Wes* of all the sampled droplets are less than 10, which confirms that shear breakup barely occurs.

As shown in Table 4, Reynolds number (Re_g) of gas-phase flow is in the magnitude of 10^5, indicating surrounding gas flow exhibits a highly turbulent status therefore droplets are inclined to break up due to the dynamic pressure fluctuations caused by the surrounding turbulence (Lasheras et al., 1998) Kolmogorov (1949). analyzed the disintegration physics of droplets under turbulent flow and stated that the disintegration of a droplet with diameter of *D* depends on three non-dimensional parameters, namely, turbulent Weber number *Wet*, scale ratio R_{sc}, and kinematic viscosity ratio R_ν (Sevik and Park, 1973), as expressed by

$$Wet = \frac{\rho_g \overline{U(D)^2} D}{\sigma}, \quad R_{sc} = \frac{D}{\eta}, \quad R_\nu = \frac{\nu_l}{\nu_g} \tag{10}$$

where $\overline{U(D)^2}$ represents the average value of the square of velocity fluctuations over two points diametrically opposite on the droplet surface. η is the Kolmogorov microscale. ν_l and ν_g are kinematic viscosities of the liquid droplet and carrier fluid (gas-phases), respectively Kolmogorov (1949). found that effect of viscosity on droplet breakup is negligible when scale ratio R_{sc} satisfies $R_{sc} \gg R_\nu^{3/4}$. At this time, the dynamic pressure caused by the ambient turbulence plays a dominant role during droplet breakup. When *Wet* is greater than a critical value of Wet_c, droplet will disintegrate because the dynamic pressure force generated by turbulent motion is sufficiently large to overcome the constraint of droplet surface tension Hinze (1955). employed Clay's experimental data of various immiscible liquids under turbulent flow to calculate the theoretical Wet_c and obtained a value close to 0.59. Additionally, Sevik and Park (1973) proposed a general expression for the critical Weber number by setting the turbulence characteristic frequency equal to the natural frequency of the second mode of spherical drop performing small amplitude oscillations. They found that the calculated critical Weber number is quite identical to the experimental results for both their investigation and Clay's observations. Besides, the obtained critical Weber number was found to be in the order of 1 and was predicted to decrease as ρ_l/ρ_g increases (Lasheras et al., 1998).

To preliminarily estimate whether turbulence breakup occurs in the gas-liquid two-phase jet involved in our application, the maximum turbulent Weber number can be calculated according to Eq. (10). Here, the maximum turbulent Weber number can be conservatively estimated according to our previous publication (Wu et al., 2021a). The $\overline{U(D)^2}$ of Eq. (10) represents the mean square of velocity differences over a distance equal to the diameter of the sample droplets across the whole jet flow field. Based on the above analysis, it is well recognized that the gas velocity can be properly characterized using tracer droplets less than 5 μm in diameter. Therefore, the velocity of these tracer droplets can be used to quantitatively estimate the fluctuating velocity of the carrier fluid with respect to the droplet surface. Furthermore, the maximum possible diameter which is characterized by D_{max} in this study is thereby used to derive the maximum probable turbulent Weber number. The resulting $\overline{U(D)^2}$ and D_{max} are then substituted into Eq. (10) to yield the maximum turbulent Weber number for turbulence breakup assessment, as listed in the last row of Table 4. What stands out in this row is that the *Wet* for both $\phi_m = 0.60$ and $\phi_m = 0.91$ exceeds 1, i.e., the order of Wet_c as mentioned above. This can be explained by the fact that the local gas-phase flow velocity of these two cases is higher than that of other cases and thus cause a more pronounced turbulence characteristic of the

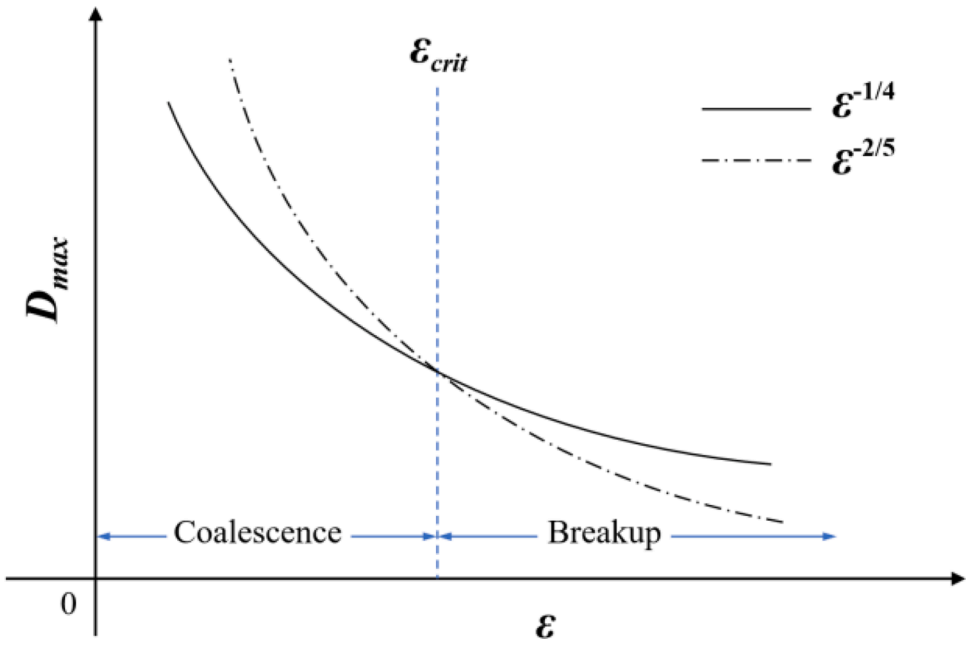

Fig. 12. Equilibrium maximum droplet diameter as a function of turbulent energy dissipation rate ε (Wu et al., 2021a).

carrier fluid. With the increasing of ϕ_m, *Wet* is found to close to the value of 0.3 since D_{max} presents an increasing function of ϕ_m. In summary, we can temporarily infer that there exists a moderate possibility for turbulent breakup occurrence of the droplets captured in the relevant operation condition.

3.5. Equilibrium analysis of turbulent break-up and coalescence

Through above analysis, we can preliminarily recognize that the droplets at $x = 50$ mm, $r = 0$ mm for all ϕ_m cases tend to undergo turbulent breakup rather than shear breakup. In this Section, a further description of the droplet behavior and dynamics concerning simultaneous breakup and coalescence of the gas-liquid two-phase jet under various ϕ_m is given based on previous theoretical studies (Wu et al., 2021a, b).

Since the time scale of droplet evaporation has been proved to be much larger than the droplet motion time scale (Ferrand et al., 2001), only the non-evaporating steady-state spray is considered thus Eq. (1) can be simplified to

$$-\nabla_x\cdot(vf) - \nabla_v\cdot(\boldsymbol{F}f) + Q_b^{'} + \Gamma_c^{'} = 0 \tag{11}$$

The velocity dependence can be eliminated by integrating Eq. (11) over the whole velocity space, yield

$$-\nabla_x\cdot(\bar{v}n) + \int Q^{'}{}_b dv + \int \Gamma^{'}{}_c dv = 0 \tag{12}$$

here $\bar{v}(r,x)$ represents the mean velocity of the droplet of radius r at location x, and $n(r,x)$ is the mean number density of droplets of radius scale r at location x, as

$$\bar{v}(r,x) = \left(\int vfdv\right) \Big/ \left(\int fdv\right),\ n(r,x) = \int fdv \tag{13}$$

Expanding the first term in Eq. (12), we get

$$\bar{v}\cdot\nabla_x n + n\nabla_x\cdot\bar{v} = Q_b + \Gamma_c \tag{14}$$

here $Q_b = \int Q^{'}{}_b dv$, and $\Gamma_c = \int \Gamma^{'}{}_c dv$. Therefore, it can be concluded that the spatial changes in the mean number density of droplets are due to the convective effect resulting from the motion of droplets in and out of the location x by virtue of their velocity $\bar{v}$, droplet breakup and coalescence (Lasheras and Hopfinger, 2000). According to the analysis in Section 3.2, the convective effect caused by the acceleration of droplets was not significant enough in the far-field. Therefore, it can be considered that the evolution of mean droplet diameter is principally dominated by the competing contributions of droplet breakup and coalescence when further neglecting the influence of the convective effect on $n(r,x)$ in Eq. (14).

Lasheras et al. (1998) measured the Sauter mean diameter (D_{32}) at different positions x along the centerline of an air-assisted liquid jet and found the downstream variation of D_{32} always shows a non-monotonic dependence which first decreases and then increases with the increasing of x. As a result, the jet field is divided into breakup and coalescence regions based on the variation of droplet D_{32}. Droplet maximum diameter in both two regions can be solely expressed by using the turbulent energy dissipation rate ε of the jet. For breakup region

$$D_{max} = \left[\frac{\sigma We_{crit}}{\rho_g}\right]^{3/5} \varepsilon^{-2/5} \tag{15}$$

and for coalescence region

$$D_{max} = C_2\varepsilon^{-1/4} \tag{16}$$

where C_2 is a constant related to gas viscosity and liquid density. Note that Eq. (15) and (16) have been explained in detail in our previous publication (Wu et al., 2021a) and more detail can also be found in the literature (Lasheras and Hopfinger, 2000). One can see that the maximum diameter of the droplet that withstands breakup is proportional to $\varepsilon^{-2/5}$. Similarly, the droplet diameter above which coalescence will be unlikely to occur is proportional to $\varepsilon^{-1/4}$. Therefore, due to the variation of ε along spray centerline and the power of ε for breakup and coalescence, the equilibrium maximum droplet diameter will be dominated by the coalescence region and breakup region, which is divided by the critical turbulent energy dissipation rate ε_{crit}, as seen in Fig. 12. For $\varepsilon < \varepsilon_{crit}$, the equilibrium maximum droplet diameter is dominated by coalescence. For $\varepsilon > \varepsilon_{crit}$, the equilibrium maximum droplet diameter is determined by breakup.

Local equilibrium can be achieved only if the droplet residence time is greater than the droplet breakup time. Otherwise, the equilibrium will

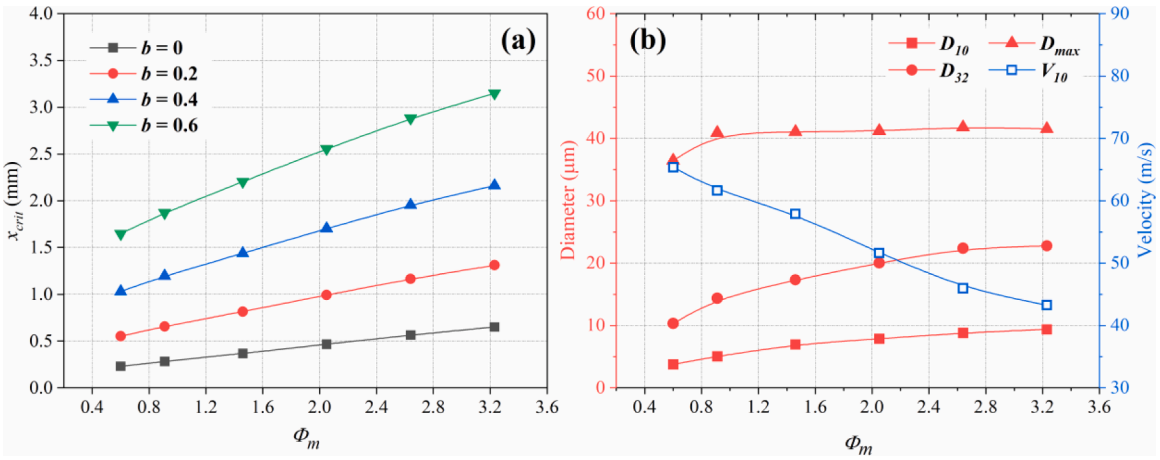

Fig. 13. (a) Critical equilibrium length under different ϕ_m values and four sets of power index b, i.e., $b = 0$, $b = 0.2$, $b = 0.4$ and $b = 0.6$. (b) Comparison of droplet size (denoted by D_{10} and D_{32}), the representative maximum diameter D_{max}, and the arithmetic mean velocity V_{10} under different ϕ_m cases.

occur at other downstream locations (Lasheras et al., 1998). Assuming that droplet breakup time is of the same magnitude as eddy turnover time which can be expressed as $t_{ed} = D_{max}/\overline{U(D)^2}^{1/2}$. Thus, introducing turbulence universal function $\overline{U(D)^2} = C_1(\varepsilon D)^{2/3}$ into the above expression yields $t_{ed} \approx \varepsilon^{-1/3} {D_{max}}^{2/3}$. To estimate droplet residence time t_{re}, gas phase velocity along the centerline of the jet is assumed to satisfy the power reduction function, as $V_g \approx V_{x=0}/x^b$, where $V_{x=0}$ is the velocity of the air-flow at the nozzle exit and b is the power index. Then the residence time of the droplet in the flow field can be calculated as

$$t_{re} = \int_0^x \frac{1}{V_g} dx = \int_0^x \frac{1}{V_{x=0}/x^b} dx \tag{17}$$

which can be integrated to get

$$t_{re} \approx \frac{x^{b+1}}{V_{x=0}(b+1)} \tag{18}$$

Therefore, $V_{x=0}$ and b must be determined in advance to calculate t_{re}. In our previous publication (Wu et al., 2021a), the corresponding $V_{x=0}$ and b were obtained by numerically fitting $V_g \approx V_{x=0}/x^b$ with discrete local gas-phase flow velocities calculated by the tracer droplet at different axial positions. In this study, we adopt the same approach to calculate the exit velocities of gas-phase for different ϕ_m conditions. Therefore, we can judge the realization of the equilibrium state according to the breakup time and residence time of the droplet when $t_{ed} = t_{re}$ (Lasheras and Hopfinger, 2000). Combining Eq. (18) and $t_{ed} \approx \varepsilon^{-1/3} {D_{max}}^{2/3}$, substituting Eq. (15) into this relation and setting the value of We_{crit} to 1, we can get the critical equilibrium location as

$$x_{crit} \approx [V_{x=0}(b+1)]^{1/(b+1)} \varepsilon^{-3/5(b+1)} \left(\frac{\sigma}{\rho_g}\right)^{2/5(b+1)} \tag{19}$$

The expression for turbulent dissipation rate ε that takes into account the presence of the liquid mass loading is proportional to the total initial flux of gas-phase kinetic energy per unit total mass, as

$$\varepsilon \approx \frac{{V_{x=0}}^3}{d_0(1+\phi_m)} \tag{20}$$

where d_0 is the equivalent diameter of the jet outlet, as $d_0 = (dl^2 - ds^2)^{1/2}$. Substituting Eq. (20) into Eq. (19), yields

$$x_{crit} \approx [V_{x=0}(b+1)]^{1/(b+1)} \left[\frac{{V_{x=0}}^3}{d_0(1+\phi_m)}\right]^{-3/5(b+1)} \left(\frac{\sigma}{\rho_g}\right)^{2/5(b+1)} \tag{21}$$

Lasheras et al. (1998) point out that the range of b is $0.2 \le b \le 0.6$, however, take the value of $b = 0$ to simplify the calculation and make a conservative estimate simultaneously in their study. Our previous experimental investigation yielded a value of 0.47 for b, which is consistent with the order of Lasheras et al.'s (1998) estimation. In this study, we discretized b into four different values (i.e., $b = 0$, $b = 0.2$, $b = 0.4$, $b = 0.6$) and analyzed their influences on x_{crit}. Note that the effects of b on the calculated $V_{x=0}$ are also fully considered in Eq. (21). The calculated critical equilibrium length under different ϕ_m, as well as discrete b are shown in Fig. 13(a). It can be found that for all selected b, x_{crit} presents an increasing function of ϕ_m. This can be explained by the fact that increase in ϕ_m leads to a decrease in the gas-phase flow velocity (see Fig. 9) and an increase in the volume of the liquid phase within the two-phase jet, resulting in a gradual shift of the critical equilibrium length downstream to the far field. Another noteworthy observation is that the power index b also has a non-negligible effect on x_{crit}, which was not fully discussed in the previous studies such as Lasheras et al. (1998) and Wu et al. (2021a). The results reveal that x_{crit} increases as b increases, which is due to the positive effect of b on $V_{x=0}$ in light of the above analysis. The maximum value of x_{crit} is unable to exceed 3.5 mm. This implies that the droplet breakup plays a major role at the position just close to the nozzle exit while the main regions of the jet are dominated by droplet coalescence, which is relatively consistent with our previous study (Wu et al., 2021a) Fig. 13(b) shows the Sauter mean diameter D_{32}, representative maximum diameter D_{max}, arithmetic mean diameter D_{10} and arithmetic mean velocity V_{10} of sampled droplets under various ϕ_m cases. An apparent positive correlation is found between ϕ_m and droplet mean diameters, while D_{max} appears to be unaffected by ϕ_m when the $\phi_m \ge 0.8$. In addition, a monotonically decreasing function of droplet average velocity with ϕ_m is noticeable. These can be understood by that increasing of ϕ_m actually suppresses jet atomization therefore produces an increase in x_{crit}, D_{10} and D_{32}.

3.6. Far-field droplet collision analysis

Summarizing the foregoing analysis, we recognized droplets in the high-intensity turbulent surrounding atmosphere may break up and coalesce simultaneously; the equilibrium location of breakup and coalescence is quite close to the nozzle exit for the jet stream we are concerned about. Coalescence caused by droplet collision is a relatively common phenomenon in the spray field formed by liquid jets (Orme, 1997). Previous investigation on the hydrocarbon droplet collision identified five distinct collision regimes in $We_c - B$ nomogram: (I) coalescence after minor deformation, (II) bouncing, (III) coalescence after substantial deformation, (IV) near head-on separation after temporary

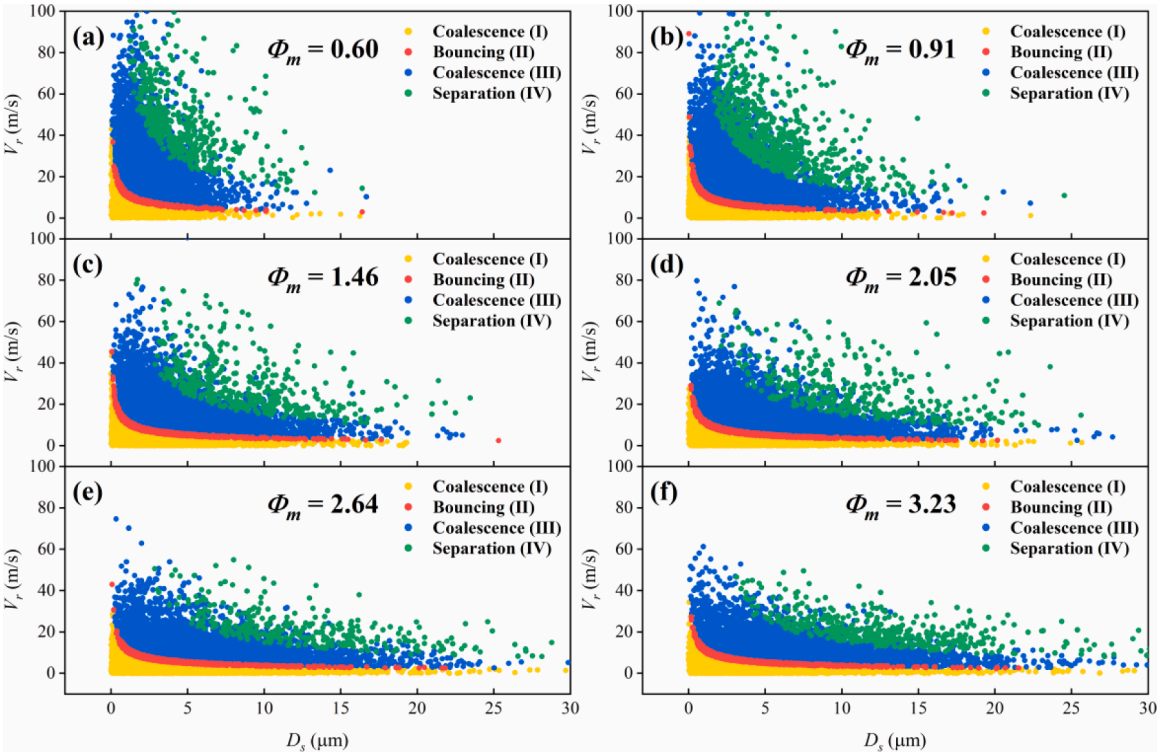

Fig. 14. Droplet collision outcome distribution under different ϕ_m cases. Note that the outcomes for each collision are marked with various colors.

coalescence and (V) off-center separation after temporary coalescence (Qian and Law, 1997). Here, B and We_c represent the collision impact parameter and collision Weber number, which are generally defined as

$$We_c = \frac{\rho_l D_s V_r^2}{\sigma}, \quad B = \frac{2\chi}{(D_L + D_s)} \tag{22}$$

where χ is the projection of the separation distance between the centers of the colliding droplets in the normal direction of droplet relative velocity V_r. Note that the case of $B = 0$ designates a head-on collision. D_L and D_s represent the diameters of a large droplet and a small droplet, respectively.

In this study, we characterize the droplet colliding dynamics based

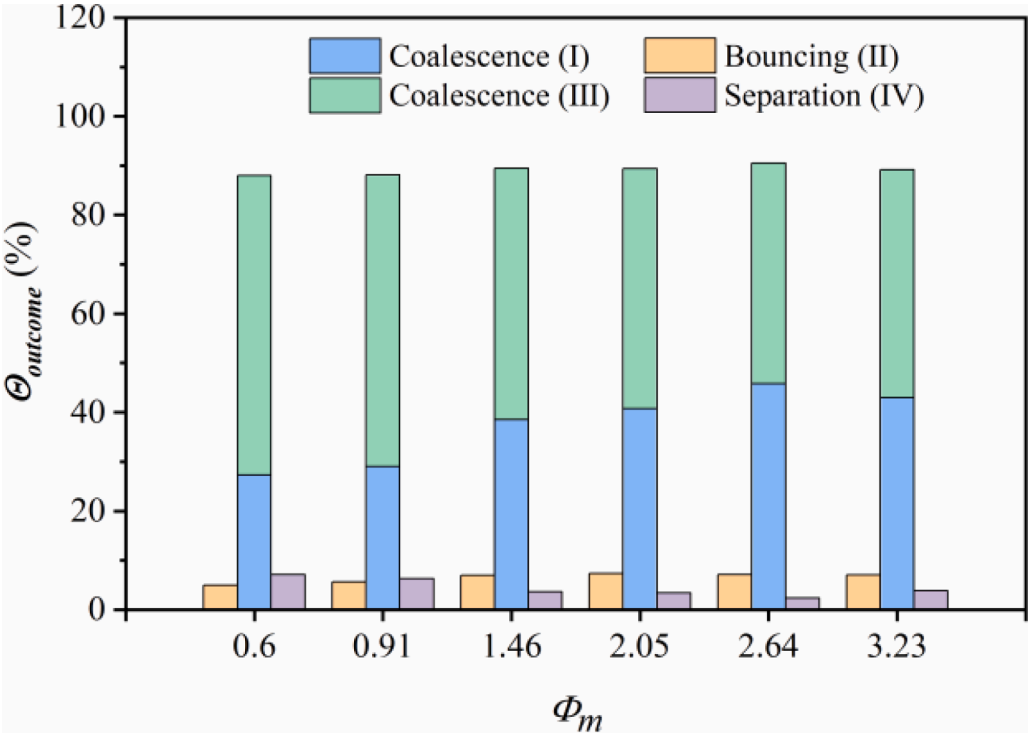

Fig. 15. Probability of various droplet collision outcomes as a function of ϕ_m.

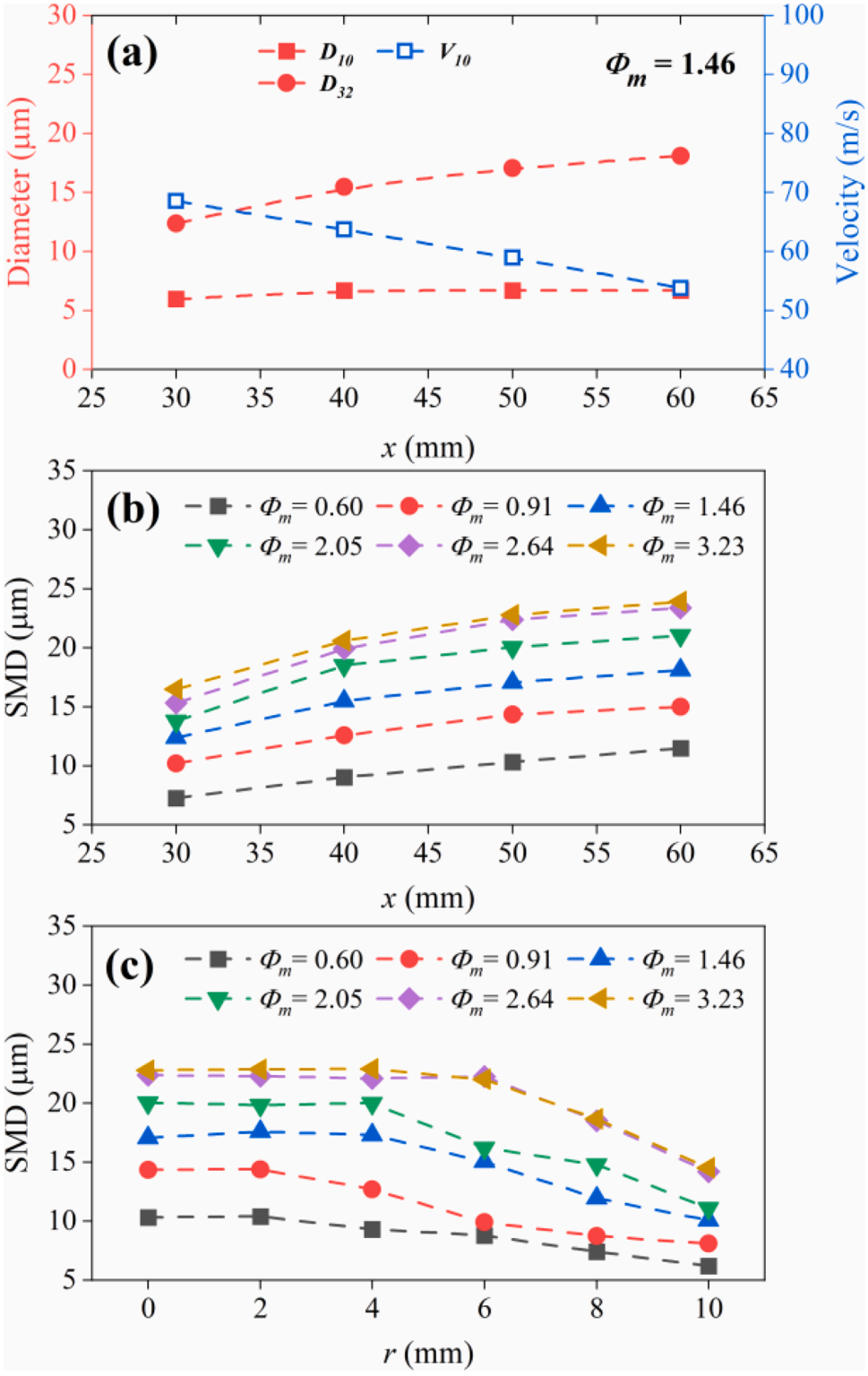

Fig. 16. (a) Downstream variation of measured droplet mean diameter (both D_{10} and D_{32}) and the arithmetic mean velocity V_{10} under the jet's centerline and a constant ϕ_m of 1.46, (b) SMD for various axial locations and (c) SMD for various radial locations as a function of mass loading ratios.

on the simplified analytical method for droplet collision in the far-field jet proposed in our previous publication (Wu et al., 2021a). First, we assumed that the droplet collision occurs only by head-on type between two adjacent droplets that are captured in sequence. Coalescence appears when the collision Weber number We_c satisfies $We_{c1} > We_c$ or $We_{c2} < We_c < We_{c3}$ based on Qian and Law's (1997) experimental results. For head-on collisions, the critical Weber numbers of transition are found to be linearly related to the liquid droplet physical parameters (the ratio of viscosity coefficient to the surface tension coefficient μ_l/σ_l) according to the experimental study of Jiang et al. (1992). The critical Weber number We_{c1} for the transition between Regimes I and II shows a decreasing function of μ_l/σ_l while We_{c2} for the transition between Regimes II and III is found to increase as μ_l/σ_l increases. In addition, collisions between unequal-size droplets are also taken into account based

on Tang et al.'s (2012) analysis, in which they concluded that size ratio slightly influence We_{c1} and We_{c2}, but substantially extends the boundary of droplet coalescence (Regime III) and separation (Regimes IV). Therefore, the theoretical model based on energy balance and scale analysis proposed by Tang et al. (2012) is adopted to revise We_{c3} and the values of We_{c1} as well as We_{c2} are referred to the diagram proposed by Qian and Law (1997), which has been described in detail in our previous work (Wu et al., 2021a).

Based on the above correction algorithm for We_{c3}, statistical calculations on the distribution of collision outcomes of sampled droplets under various ϕ_m cases are performed in the parameter space of V_r and D_s, as shown in Fig. 14. It should be noted that coalescence here is divided into two situations, namely soft coalescence (abbreviated to coalescence I), and hard coalescence (abbreviated to coalescence III). It is clearly seen that droplet collisions tend to coalesce with minor deformation when the relative velocity V_r or droplet size ratio D_s is small. As V_r or D_s increases, collision outcomes will experience bouncing (II), hard coalescence (III), and separation (IV) in order. To quantify the collision outcomes, Fig. 15 depicts the calculated probability of collision outcomes $\Theta_{outcome}$ for different ϕ_m values. Overall, the probability of coalescence, including both soft and hard coalescence, is obviously higher than the other outcomes. These results are quite similar to those obtained by Saha et al. (2012) for swirling jet. Besides, $\Theta_{outcome}$ of soft coalescence shows an increasing function of ϕ_m, while $\Theta_{outcome}$ for hard coalescence is a decreasing function of ϕ_m. The main reason for this observation is the significant decrease in droplet velocity due to the increase of ϕ_m, which in turn leads to a decrease in the relative velocity of the colliding droplets, resulting in a decrease in the collision Weber number. From the evaluated results, it is believed that there is a remarkable possibility of coalescence for droplets downstream of the jet, which is consistent with previous Section 3.5 about the droplet breakup and coalescence equilibrium analysis.

Fig. 16(a) shows the variation of droplet mean diameter (both D_{10} and D_{32}) and the arithmetic mean velocity V_{10} with the downstream location x along the jet's centerline at $\phi_m = 1.46$. Under a constant mass loading ratio condition, the D_{32} shows a notable increasing function with axial location x, which is attributed to the high droplet coalescence probability in the jet far-field. Hence, for the high-speed gas-liquid two-phase jet involved in this study, the droplet breakup process is fundamentally completed in the jet near-field, while the droplet size in the far-field is principally dominated by droplet coalescence.

The SMD for different axial and radial locations under various mass loading ratios are shown in Fig. 16(b) and 16(c), respectively Fig. 16.(b) shows that, for all mass loading ratios, the SMD increases monotonously with axial location. This is somewhat expected. Since droplet collision and coalescence dominate the droplet dynamic of far-field spray (Lasheras et al., 1998; Saha et al., 2012), the droplet size will tend to increase progressively. Also, under the same axial location, a significant incremental trend of SMD with mass loading ratio can be observed. This can be attributed to the increasing quantity of delivered liquid within the gas-liquid two-phase jet. It should also be noted that the difference in axial SMD between $\phi_m = 2.64$ and $\phi_m = 3.23$ is relatively inconspicuous, implying a potential limited dependence of mass loading ratio on droplet SMD. Regarding the dependence of mass loading ratio on SMD, the same results can be found for various radial locations, as shown in Fig. 16(c). In addition, for all mass loading ratios, the radial SMD is nearly constant near spray axis and then decreases with the increasing of radial location. This implies that droplet collisions are more frequent at the spray axis due to the presence of more droplets. Moreover, the width of this near-axis high-frequency droplet collision region is found to be positively correlated with mass loading ratio. This observation can be explained again by the increasing number of droplets caused by more delivered liquid and the simultaneous increase in the radial width of the spray (Wu et al., 2021b).

4. Conclusions

Simultaneous measurements of droplet size and velocity under various liquid mass loading ratios were carried out to investigate the fundamental atomization characteristics, spray droplet dynamics, as well as droplet-gas interactions of a droplet-laden two-phase jet issuing from an internal-mixing twin-fluid pulsed atomizer. Sufficient discrete spray droplets were sampled at fixed locations in the jet field and used for comparison and analysis. The main findings are summarized as follows.

Droplet floating average velocity generally tends to be flatter as a function of droplet diameter under various ϕ_m cases, indicating that droplets of various size classes have reached the local gas-phase flow velocity at the sampling location ($x = 50$ mm, $r = 0$ mm). The calculated Pearson correlation coefficient between droplet velocity and diameter did not exceed 0.3, proving that there was no significant correlation between these two parameters. The downstream evolution of mean droplet velocity can be divided into three regions based on mean slip velocity, namely acceleration, velocity overshooting, and deceleration. The boundaries of these regions show substantial ϕ_m–dependent characteristics, indicating droplet transport characteristic is substantially influenced by the mass load ratio. The represented gas velocity shows a decreasing function of ϕ_m, and the Reynolds number of gas-phase is found to exceed the order of 5×10^4, indicating a highly turbulent state.

Evaluation of the droplet breakup reveals that droplets are essentially immune to shear breakup, but may further undergo turbulent breakup. Based on the theoretical study of Lasheras et al. (1998) and our previous analysis (Wu et al., 2021a), the critical equilibrium location x_{crit} between droplet turbulent breakup and coalescence is found to be quite close to the nozzle exit for all ϕ_m conditions. This suggests that jet atomization in the far field is principally dominated by droplet collisions. The quantified colliding outcomes based on classical binary droplet collision theory indicate that the possibility of droplet coalescence dominates and thus the droplet Sauter mean diameter shows a positive correlation with downstream location x in the jet's far-field.

CRediT authorship contribution statement

Hao Wu: Conceptualization, Validation, Formal analysis, Investigation, Visualization, Writing – original draft, Methodology, Formal analysis, Resources. **Fujun Zhang:** Methodology, Supervision, Resources. **Zhenyu Zhang:** Writing – review & editing, Supervision, Project administration, Funding acquisition, Methodology, Supervision. **Lin Hou:** Methodology, Resources.

Declaration of Competing Interest

None.

Acknowledgments

The authors would like to acknowledge the research grant received from the National Natural Science Foundation of China (grant no. 51806013), Foundation research funds of the Ministry of Industry and Information Technology (grant no. JCKY2019602D018 and WDZC-2019-JGKK-02), and the Beijing Institute of Technology Research Fund Program for Young Scholars (grant no. 2020CX04047).

References

Albrecht, H.-E., Damaschke, N., Borys, M., Tropea, C., 2013. Laser Doppler and phase Doppler measurement techniques. Springer Science & Business Media.
Balachandar, S., Eaton, J.K., 2009. Turbulent dispersed multiphase flow. Annu. Rev. Fluid Mech 42, 111–133.
Bayvel, L., 1993. Liquid atomization. CRC Press.

Beale, J.C., Reitz, R.D., 1999. Modeling spray atomization with the Kelvin-Helmholtz/Rayleigh-Taylor hybrid model. Atom. Sprays 9, 623–650.
Brazier-Smith, P., Jennings, S., Latham, J., 1972. The interaction of falling water drops: coalescence. Proc. R. Soc. London, Ser. A 326, 393–408.
Crowe, C.T., Schwarzkopf, J.D., Sommerfeld, M., Tsuji, Y., 2011. Multiphase flows with droplets and particles. CRC Press, Boca Raton.
Doudou, A., 2005. Turbulent flow study of an isothermal diesel spray injected by a common rail system. Fuel 84, 287–298.
Drui, F., Larat, A., Kokh, S., Massot, M., 2019. Small-scale kinematics of two-phase flows: identifying relaxation processes in separated- and disperse-phase flow models. J. Fluid Mech 876, 326–355.
Feng, Z., Tang, C., Yin, Y., Zhang, P., Huang, Z., 2019. Time-resolved droplet size and velocity distributions in a dilute region of a high-pressure pulsed diesel spray. Int. J. Heat Mass Transfer 133, 745–755.
Ferrand, V., Bazile, R., Borée, J., 2001. Measurements of concentration per size class in a dense polydispersed jet using planar laser-induced fluorescence and phase Doppler techniques. Exp. Fluids 31, 597–607.
Ferrand, V., Bazile, R., Borée, J., Charnay, G., 2003. Gas–droplet turbulent velocity correlations and two-phase interaction in an axisymmetric jet laden with partly responsive droplets. Int. J. Multiphase Flow 29, 195–217.
Gao, H., Zhang, F., Zhang, Z., Wang, S., Wu, H., 2019. Trajectory deviation of target jet of air-assisted spray under different conditions. Fuel 249, 252–263.
Gorokhovski, M., Herrmann, M., 2008. Modeling primary atomization. Annu. Rev. Fluid Mech 40, 343–366.
Guildenbecher, D.R., López-Rivera, C., Sojka, P.E., 2009. Secondary atomization. Exp. Fluids 46, 371.
Hinze, J.O., 1955. Fundamentals of the hydrodynamic mechanism of splitting in dispersion processes. AIChE J 1, 289–295.
Jebakumar, A.S., Abraham, J., 2016. Comparison of the structure of computed and measured particle-laden jets for a wide range of Stokes numbers. Int. J. Heat Mass Transfer 97, 779–786.
Jedelsky, J., Jicha, M., 2013. Energy conversion during effervescent atomization. Fuel 111, 836–844.
Jedelsky, J., Maly, M., Pinto del Corral, N., Wigley, G., Janackova, L., Jicha, M., 2018. Air–liquid interactions in a pressure-swirl spray. Int. J. Heat Mass Transfer 121, 788–804.
Jiang, X., Siamas, G.A., Jagus, K., Karayiannis, T.G., 2010. Physical modelling and advanced simulations of gas–liquid two-phase jet flows in atomization and sprays. Prog. Energy Combust. Sci. 36, 131–167.
Jiang, Y.J., Umemura, A., Law, C.K., 1992. An experimental investigation on the collision behaviour of hydrocarbon droplets. J. Fluid Mech 234, 171–190.
Kannaiyan, K., Sadr, R., 2014. Experimental investigation of spray characteristics of alternative aviation fuels. Energy Convers. Manage. 88, 1060–1069.
Kolmogorov, A.N., 1949. On the disintegration of drops by turbulent flows. Dokl. Akad. Nauk. SSSR 66, 825–828.
Kourmatzis, A., Masri, A.R., 2014. Air-assisted atomization of liquid jets in varying levels of turbulence. J. Fluid Mech 764, 95–132.
Lasheras, J.C., Hopfinger, E.J., 2000. Liquid jet instability and atomization in a coaxial gas stream. Annu. Rev. Fluid Mech 32, 275–308.
Lasheras, J.C., Villermaux, E., Hopfinger, E.J., 1998. Break-up and atomization of a round water jet by a high-speed annular air jet. J. Fluid Mech 357, 351–379.
Lau, T.C.W., Nathan, G.J., 2014. Influence of Stokes number on the velocity and concentration distributions in particle-laden jets. J. Fluid Mech 757, 432–457.
Lefebvre, A.H., McDonell, V.G., 2017. Atomization and sprays. CRC press.
Li, Z., Wu, Y., Yang, H., Cai, C., Zhang, H., Hashiguchi, K., Takeno, K., Lu, J., 2013. Effect of liquid viscosity on atomization in an internal-mixing twin-fluid atomizer. Fuel 103, 486–494.
Lin, S.P., Reitz, R.D., 1998. Drop and spray formation from a liquid jet. Annu. Rev. Fluid Mech 30, 85–105.
Manish, M., Sahu, S., 2019. Droplet clustering and local spray unsteadiness in air-assisted sprays. Exp. Therm Fluid Sci. 100, 89–103.
Mashayek, F., Pandya, R.V.R., 2003. Analytical description of particle/droplet-laden turbulent flows. Prog. Energy Combust. Sci. 29, 329–378.
Mlkvik, M., Stähle, P., Schuchmann, H.P., Gaukel, V., Jedelsky, J., Jicha, M., 2015. Twin-fluid atomization of viscous liquids: The effect of atomizer construction on breakup process, spray stability and droplet size. Int. J. Multiphase Flow 77, 19–31.
Orme, M., 1997. Experiments on droplet collisions, bounce, coalescence and disruption. Prog. Energy Combust. Sci. 23, 65–79.
Pilch, M., Erdman, C.A., 1987. Use of breakup time data and velocity history data to predict the maximum size of stable fragments for acceleration-induced breakup of a liquid drop. Int. J. Multiphase Flow 13, 741–757.
Pope, S.B., 2000. Turbulent Flows. Cambridge University Press.
Prevost, F., Boree, J., Nuglisch, H.J., Charnay, G., 1996. Measurements of fluid/particle correlated motion in the far field of an axisymmetric jet. Int. J. Multiphase Flow 22, 685–701.
Qian, J., Law, C.K., 1997. Regimes of coalescence and separation in droplet collision. J. Fluid Mech 331, 59–80.
Rajamanickam, K., Basu, S., 2016. Insights into the dynamics of spray–swirl interactions. J. Fluid Mech 810, 82–126.
Reitz, R.D., Liu, A.B., 1993. Mechanisms of air-assisted liquid atomization. Atom. Sprays 3, 55–75.
Saha, A., Lee, J.D., Basu, S., Kumar, R., 2012. Breakup and coalescence characteristics of a hollow cone swirling spray. Phys. Fluids 24, 124103.
Sevik, M., Park, S.H., 1973. The splitting of drops and bubbles by turbulent fluid flow. J. Fluids Eng. 95, 53–60.
Sharma, P., Fang, T., 2015. Spray and atomization of a common rail fuel injector with non-circular orifices. Fuel 153, 416–430.
Sommerfeld, M., Pasternak, L., 2019. Advances in modelling of binary droplet collision outcomes in Sprays: A review of available knowledge. Int. J. Multiphase Flow 117, 182–205.
Sovani, S.D., Sojka, P.E., Lefebvre, A.H., 2001. Effervescent atomization. Prog. Energy Combust. Sci. 27, 483–521.
Tang, C., Zhang, P., Law, C.K., 2012. Bouncing, coalescence, and separation in head-on collision of unequal-size droplets. Phys. Fluids 24, 022101.
Tropea, C., Yarin, A.L., 2007. Springer handbook of experimental fluid mechanics. Springer Science & Business Media.
Urbán, A., Zaremba, M., Malý, M., Józsa, V., Jedelský, J., 2017. Droplet dynamics and size characterization of high-velocity airblast atomization. Int. J. Multiphase Flow 95, 1–11.
Vadivukkarasan, M., Panchagnula, M.V., 2016. Combined Rayleigh–Taylor and Kelvin–Helmholtz instabilities on an annular liquid sheet. J. Fluid Mech 812, 152–177.
Varga, C.M., Lasheras, J.C., Hopfinger, E.J., 2003. Initial breakup of a small-diameter liquid jet by a high-speed gas stream. J. Fluid Mech 497, 405–434.
Wang, F., Fang, T., 2015. Liquid jet breakup for non-circular orifices under low pressures. Int. J. Multiphase Flow 72, 248–262.
Wang, L., Lowrie, J., Ngaile, G., Fang, T., 2019. High injection pressure diesel sprays from a piezoelectric fuel injector. Appl. Therm. Eng. 152, 807–824.
Warner, R.M., 2012. Applied statistics: From bivariate through multivariate techniques. Sage Publications.
Williams, F.A., 2018. Combustion theory. CRC Press.
Wu, H., Zhang, F., Zhang, Z., 2021a. Droplet breakup and coalescence of an internal-mixing twin-fluid spray. Phys. Fluids 33, 013317.
Wu, H., Zhang, F., Zhang, Z., 2021b. Fundamental spray characteristics of air-assisted injection system using aviation kerosene. Fuel 286, 119420.
Wu, H., Zhang, F., Zhang, Z., Gao, H., 2020a. Experimental investigation on the spray characteristics of a self-pressurized hollow cone injector. Fuel 272, 117710.
Wu, H., Zhang, F., Zhang, Z., Guo, Z., Zhang, W., Gao, H., 2020b. On the role of vortex-ring formation in influencing air-assisted spray characteristics of n-heptane. Fuel 266, 117044.
Zaremba, M., Weiß, L., Malý, M., Wensing, M., Jedelský, J., Jícha, M., 2017. Low-pressure twin-fluid atomization: Effect of mixing process on spray formation. Int. J. Multiphase Flow 89, 277–289.
Zhang, Z., Chi, Y., Shang, L., Zhang, P., Zhao, Z., 2016. On the role of droplet bouncing in modeling impinging sprays under elevated pressures. Int. J. Heat Mass Transfer 102, 657–668.
Zhang, Z., Zhang, P., 2017. Kinetic energy recovery and interface hysteresis of bouncing droplets after inelastic head-on collision. Phys. Fluids 29, 103306.